J. Fluid Mech. (1995), *vol.* 298, *pp.* 211–248

Direct numerical simulation of controlled transition in a flat-plate boundary layer

By U. RIST[1] AND H. FASEL[2]

[1] Institut für Aero- und Gasdynamik, Universität Stuttgart, D-70550 Stuttgart, Germany
[2] Department of Aerospace and Mechanical Engineering, The University of Arizona, Tucson, AZ 85721, USA

(Received 1 September 1993 and in revised form 18 August 1994)

The three-dimensional development of controlled transition in a flat-plate boundary layer is investigated by direct numerical simulation (DNS) using the complete Navier–Stokes equations. The numerical investigations are based on the so-called spatial model, thus allowing realistic simulations of spatially developing transition phenomena as observed in laboratory experiments. For solving the Navier–Stokes equations, an efficient and accurate numerical method was developed employing fourth-order finite differences in the downstream and wall-normal directions and treating the spanwise direction pseudo-spectrally. The present paper focuses on direct simulations of the wind-tunnel experiments by Kachanov *et al.* (1984, 1985) of fundamental breakdown in controlled transition. The numerical results agreed very well with the experimental measurements up to the second spike stage, in spite of relatively coarse spanwise resolution. Detailed analysis of the numerical data allowed identification of the essential breakdown mechanisms. In particular, from our numerical data, we could identify the dominant shear layers and vortical structures that are associated with this breakdown process.

1. Introduction

In spite of considerable research efforts over the last fifty years, laminar–turbulent transition is still far from being understood. This is particularly true for 'open' or 'inflow–outflow' systems, such as boundary layers, considered here. For open-flow systems, transition is a *spatially* evolving process, where in 'real' situations (natural transition), the transition process is initiated by environmental disturbances such as pressure fluctuations, vortical free-stream disturbances, sound, small-scale free-stream turbulence, etc. By virtue of certain receptivity mechanisms, which for wall boundary layers are enhanced by strong, local geometric variations such as steps, protuberances (roughness), suction slots or holes, locally strong pressure gradients, etc., the environmental disturbances generate instability waves within the boundary layers that can grow while propagating downstream and eventually leading to the breakdown to turbulence. Thus, the breakdown to turbulence is a consequence of the disturbance input into the flow system, e.g. the boundary layer.

Therefore, in an ideal situation completely void of any disturbances, the transition process in a boundary layer flow could not evolve or, if already underway, would come to a halt and the flow would relax to a laminar undisturbed state, no matter how strongly 'unstable' the laminar base flow may be. This fundamental behaviour must have already been clearly understood by Schubauer & Skramstad (1947), who realized that a reduction of the environmental disturbance level (i.e. of free-stream turbulence) was crucial in order to be able to observe and study the transition process initiated by small-amplitude (linear) instability waves (Tollmien–Schlichting waves). After considerable reduction of the free-stream turbulence level of their wind tunnel, so-called 'controlled' experiments could be conducted where transition was initiated by small two-dimensional disturbance waves that were produced by a vibrating ribbon. With these controlled transition experiments, it could be verified that the breakdown to turbulence is indeed a consequence of local disturbance input. Because of this direct dependence of the local state of the transition development on the disturbance input, controlled experiments (with the transition development triggered by controlled forcing) have been employed ever since for investigating transition (see, for example, Klebanoff, Tidstrom & Sargent 1962; Hama & Nutant 1963; Kachanov & Levchenko 1984).

From advances in theoretical understanding (Gaster 1968; Huerre & Monkewitz 1990), today we know that this behaviour of the disturbance waves is due to the *convective* stability property of certain open flows, of which the boundary layer is an example. This is in contrast to the absolute stability property of closed flows (i.e. Taylor–Couette flow or Bénard convection), where an initial, one-time excitation may be sufficient to carry the flow all the way from the laminar to the turbulent state provided that a characteristic stress parameter (such as the Reynolds number or Rayleigh number) is large enough so that the linear stability limit is exceeded. A detailed discussion of the issues concerning convective and absolute instability is presented in the review paper by Huerre & Monkewitz (1990).

It is known from the experiments of Schubauer & Skramstad (1947) that the first stage of the transition process consists of the amplification of two-dimensional waves that propagate in the downstream direction. The amplitude growth and propagation speed of these disturbance waves depends on the frequency and Reynolds number. The development of these waves is well described by linear stability theory (Heisenberg 1924; Tollmien 1929; Schlichting 1933), which at first was formulated based on a temporal model. Therefore, Schubauer & Skramstad used the phase velocity of the disturbance waves to enable comparison of their measurements with the theory. Later, however, Gaster (1962) showed that the use of the phase velocity for relating the temporal development of the theory with the spatial development of the experiments was only approximately correct. Owing to a suggestion by Gaster (1965*a*, *b*), the stability problem was then reformulated as a spatial one (see, for example, Jordinson 1970), which then allowed direct comparison of theory with experiments.

After the two-dimensional disturbance waves (Tollmien–Schlichting waves) reach certain amplitude levels, pronounced three-dimensional developments set in, which then rapidly lead to breakdown to a random, turbulent motion. Such three-dimensional developments had already been observed by Schubauer & Skramstad. In subsequent controlled experimental investigations by various researchers, the three-dimensional processes were studied in great detail (see, for example, Klebanoff *et al.* 1962; Kovasznay, Komoda & Vasudeva 1962; Hama & Nutant 1963; Kachanov & Levchenko 1984).

From such experiments, two basic three-dimensional transition mechanisms were identified, namely (*a*) the so-called fundamental breakdown, which was first found experimentally by Klebanoff *et al.* (1962), and (*b*) the subharmonic breakdown, which was first identified by Kachanov, Kovloz & Levchenko (1977).† The onset of the three-dimensionality by both the fundamental and subharmonic breakdown was later explained by a secondary instability mechanism (see Herbert 1988), where the boundary layer flow and a superposed finite amplitude Tollmien–Schlichting wave form a new base flow. This new base flow can then be unstable to three-dimensional (oblique) disturbances of the same frequency as the fundamental (two-dimensional) wave ('fundamental breakdown') or of half the frequency of the fundamental (two-dimensional) wave ('subharmonic breakdown'). Variations of these two basic breakdown scenarios can occur when the two- and three-dimensional disturbances are 'detuned'.

The secondary instability model describes the onset of three-dimensionality quite well. However, owing to the simplifying assumptions in this theory (in particular, that the three-dimensional disturbances are small) in order to enable linearization of the resulting disturbance equations, the ensuing three-dimensional development cannot be captured adequately. Therefore, in the present paper, direct numerical simulations (DNS) based on the complete Navier–Stokes equations are employed in an attempt to investigate the three-dimensional transition development beyond its onset. In our DNS approach, no restricting assumptions are necessary with regard to the base flow and the ensuing disturbance flow. In particular, the model employed here is spatial, so that both the spatial base flow and the spatial disturbance flow development as observed in experiments can be realistically modelled.

In contrast, past attempts to simulate transition were mostly based on the so-called 'temporal' model (see, for example, Kleiser 1982; Laurien & Kleiser 1989; Wray & Hussaini 1984; Spalart & Yang 1987; Zang & Hussaini 1987). Employing either the spatial or the temporal model has very different implications for transition simulations. In the widely used temporal model, the flow is assumed to be spatially periodic so that identical flow conditions (periodicity) can be used at the inflow and outflow boundary of an integration domain that contains an integer multiple of the fundamental wavelength. Then, the development of the flow, for both the disturbance flow and the base flow (which is often kept constant) is temporal, i.e. the disturbances grow or decay in time, dependent upon whether the base flow is unstable or stable, respectively. Thus, the flow responds much like a 'closed' flow system that possesses an absolute instability. Because the base flow is then invariant with respect to the downstream coordinate, the model cannot account for so-called non-parallel effects.

When employing the temporal model, exploiting the downstream periodicity allows the use of spectral or pseudo-spectral approximations in the downstream direction which results in very efficient numerical methods. In addition, with the typically much smaller downstream extent of the computational domain compared to the spatial model, simulations based on the temporal model are generally less demanding with respect to algorithmic efficiency and computer hardware requirements (memory and speed). For these reasons, in most transition simulations in the past, the temporal model was used. For cases of controlled transition, reasonable agreement was achieved, although quantitative comparisons with experimental measurements were somewhat ambiguous. The disadvantages of the temporal approach result from the underlying assumptions. Therefore, in situations where these assumptions are not justified, for example when strong spatial variation of the base flow exists (caused by strong pressure gradients, local geometric variations, such as steps, bumps, flow

---

† The discussion of an alternative route leading to transition involving oblique waves (cf. Schmidt & Henningson 1992) is omitted, since there is no evidence that such a mechanism is relevant for the transition scenery of the Kachanov experiments addressed in this paper.

separation, etc.), or when the upstream feedback is important, the temporal model should not be employed.

The spatial model, on the other hand, is physically realistic in that it allows both the base flow and disturbance flow to develop in the downstream direction, as in the laboratory experiments or in practical applications. Thus, in the spatial model, non-parallel effects are included, allowing, in particular, interactions between non-parallel and nonlinear effects. The response of the flow field (in both the upstream and downstream directions) to local disturbance sources can be studied. It is therefore applicable for receptivity studies whereas the temporal model really is not. The spatial model is particularly well suited for simulations of controlled transition experiments, where the transition developments are in fact a consequence of forcing by local disturbance sources.

The disadvantages of the spatial model result from the fact that it is computationally much more demanding than the temporal model. Spatial transition simulations are therefore relatively scarce in the literature. A successful example is the spatial simulation of flat-plate bypass transition by Rai & Moin (1993) using a finite-difference scheme on a zonal grid system. Difficulties result largely from the outflow boundary conditions, which are difficult to specify and implement, so that unhindered passage of the disturbances is possible without adversely effecting the computations upstream of the boundary. (For a detailed discussion of the difficulties associated with outflow boundary conditions, see Kloker, Konzelmann & Fasel 1993.) In addition, the spatial simulations require a much larger downstream extension of the domain, thus placing high demands on algorithmic efficiency of the Navier–Stokes method in order to be able to carry out such simulations with the supercomputers available today. For additional detailed discussions concerning numerical aspects of transition simulations, see the recent review by Kleiser & Zang (1991). More recently, a different method based on the parabolized stability equations for the investigation of spatially developing disturbances was developed by Herbert and Bertolotti. Their results compared favourably with existing data (see, e.g. Bertolotti 1991; Bertolotti, Herbert & Spalart 1992), and may be further checked against the results presented in this paper.

In this paper, we will present and discuss results of direct numerical simulations based on the spatial model of the transition experiments of Kachanov *et al.* (1984). We believe that these results will demonstrate that direct numerical simulations based on the spatial model can be achieved with a degree of accuracy and reliability not thought possible before.

A somewhat different transition scenario, also resulting from a controlled disturbance input where the transition process was initiated by pulse-like disturbances, was investigated both theoretically and experimentally by Gaster & Grant (1975). These pulse disturbances were introduced into the boundary layer through a small circular hole. Thus, in this case, a three-dimensional disturbance development is present from the outset and therefore plays an even greater role. This scenario will not be discussed here, but will be addressed in a subsequent paper.

2. Governing equations; boundary and initial conditions

The numerical model is based on the complete Navier–Stokes equations for incompressible three-dimensional unsteady flow. These equations, together with an appropriate set of boundary and initial conditions, are solved numerically in a computational domain, as shown schematically in figure 1. In the numerical model, all variables are used in dimensionless form. The dimensional variables, denoted by a

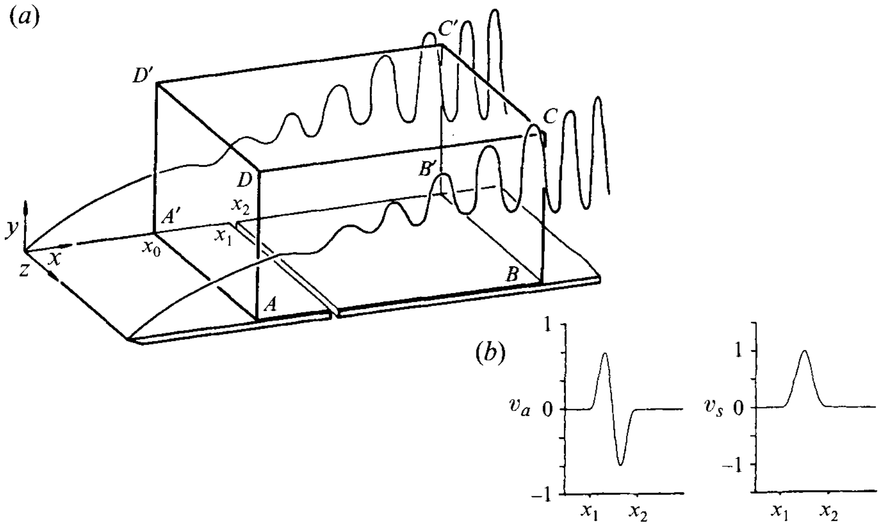

FIGURE 1. Schematic representation of the problem: (*a*) computational domain; (*b*) v-velocity distribution over blowing and suction strip for generating disturbances.

tilde, are non-dimensionalized using a reference length $\tilde{L}$ and the free-stream velocity $\tilde{U}_\infty$. Then, the non-dimensional variables relate to their corresponding dimensional counterparts as follows:

$$\left.\begin{aligned} x=\frac{\tilde{x}}{\tilde{L}},\quad y=\frac{\tilde{y}}{\tilde{L}}Re^{1/2},\quad z=\frac{\tilde{z}}{\tilde{L}},\quad t=\tilde{t}\frac{\tilde{U}_\infty}{\tilde{L}},\\ u=\frac{\tilde{u}}{\tilde{U}_\infty},\quad v=\frac{\tilde{v}}{\tilde{U}_\infty}Re^{1/2},\quad w=\frac{\tilde{w}}{\tilde{U}_\infty},\end{aligned}\right\} \tag{1}$$

with the Reynolds number defined as $Re=\tilde{U}_\infty\tilde{L}/\tilde{\nu}$ ($\tilde{\nu}$ is the kinematic viscosity).

In the numerical model, the Navier–Stokes equations are used in a vorticity–velocity formulation (Fasel 1976) using the three vorticity components and three velocity components as dependent variables. With the non-dimensionalization introduced above, the non-dimensional vorticity components are given as

$$\omega_x=\frac{1}{Re}\frac{\partial v}{\partial z}-\frac{\partial w}{\partial y},\quad \omega_y=\frac{\partial w}{\partial x}-\frac{\partial u}{\partial z},\quad \omega_z=\frac{\partial u}{\partial y}-\frac{1}{Re}\frac{\partial v}{\partial x}. \tag{2}$$

Also, in the numerical model employed here, the Navier–Stokes equations are used in a 'disturbance formulation'; that is, for the calculation of the disturbed flow field, the disturbance variables are used as the dependent variables and not the total variables as in a 'total variable formulation'. Towards this end, the total flow field is decomposed into a steady two-dimensional base flow (with flow variables denoted by subscript B) and an unsteady three-dimensional disturbance flow (with variables denoted by a prime). Thus, with capital bold-faced letters denoting vectors, we have

$$\left.\begin{aligned} \boldsymbol{V}&=\boldsymbol{V}_B(x,y)+\boldsymbol{V}'(x,y,z,t),\\ \boldsymbol{\Omega}&=\boldsymbol{\Omega}_B(x,y)+\boldsymbol{\Omega}'(x,y,z,t),\end{aligned}\right\} \tag{3}$$

with

$$\boldsymbol{V}_B=\{u_B,v_B,0\},\quad \boldsymbol{\Omega}_B=\{0,0,\omega_{z_B}\},$$

$$\boldsymbol{V}'=\{u',v',w'\},\quad \boldsymbol{\Omega}'=\{\omega_x',\omega_y',\omega_z'\}.$$

It should be noted, however, that this decomposition was not introduced for the sake of a later linearization, as in the customary derivation of the linear stability theory equations. Rather, it was introduced to facilitate implementation of the boundary conditions at the free-stream and outflow boundaries. In the present model, there is no linearization and therefore nonlinear effects are considered fully, so that the effects of nonlinearity on the disturbance flow or on the steady mean flow are accounted for entirely.

The *mean flow* (denoted by overbars), in contrast to the *base flow*, is obtained from the time-averaged disturbance flow:

$$\bar{\boldsymbol{V}} = \boldsymbol{V}_B + \overline{\boldsymbol{V}'}, \quad \bar{\boldsymbol{\Omega}} = \boldsymbol{\Omega}_B + \overline{\boldsymbol{\Omega}'}, \tag{4}$$

with

$$\bar{\boldsymbol{V}} = \{\bar{u}, \bar{v}, \bar{w}\}, \quad \bar{\boldsymbol{\Omega}} = \{\bar{\omega}_x, \bar{\omega}_y, \bar{\omega}_z\},$$

$$\overline{\boldsymbol{V}'} = \{\overline{u'}, \overline{v'}, \overline{w'}\}, \quad \overline{\boldsymbol{\Omega}'} = \{\overline{\omega'_x}, \overline{\omega'_y}, \overline{\omega'_z}\}.$$

The time average is taken over a suitable time period; in the present case, it is over one or more integer multiples of the period of the disturbance input.

For the present investigations, the steady base flow is obtained from numerical solution of the Navier–Stokes equations before the calculations of the unsteady flow field are initiated. For other situations where exact (or accurate) solutions of the base flow are available (such as for plane Poiseuille flow), these solutions could, of course, be taken as the base flow directly. However, for a flat-plate boundary layer, as in this case, small differences between the Blasius similarity solution and a numerical Navier–Stokes solution do exist. In order to avoid any possible ambiguities caused by these differences, albeit minor, we are using the Navier–Stokes solution because it adds little to the entire cost of the numerical simulations.

2.1. *Calculation of the base flow*

2.1.1. *Governing equations*

As mentioned above, in the present investigations, the Navier–Stokes equations are used in a vorticity–velocity formulation (see Fasel 1976) with a vorticity transport equation for ω_{z_B},

$$\frac{\partial}{\partial x}(u_B \omega_{z_B}) + \frac{\partial}{\partial y}(v_B \omega_{z_B}) = \frac{1}{Re}\frac{\partial^2 \omega_{z_B}}{\partial x^2} + \frac{\partial^2 \omega_{z_B}}{\partial y^2}, \tag{5a}$$

and a Poisson-type equation for v_B,

$$\frac{1}{Re}\frac{\partial^2 v_B}{\partial x^2} + \frac{\partial^2 v_B}{\partial y^2} = -\frac{\partial \omega_{z_B}}{\partial x}, \tag{5b}$$

while u_B is calculated from

$$\frac{\partial^2 u_B}{\partial x^2} = -\frac{\partial^2 v_B}{\partial x\,\partial y}. \tag{5c}$$

Equation (5*a*) is in a so-called 'conservative' form (conserving vorticity; see Roache 1976). Equations (5*b*) and (5*c*) are obtained from the definition of vorticity (2) and the continuity equation.

2.1.2. *Boundary conditions*

The steady base flow is calculated in the rectangular integration domain *ABCD* (see figure 1*a*) using the following boundary conditions. At the inflow boundary ($x = x_0$), we prescribe a Blasius boundary layer flow (denoted by index *Bl*):

$$u_B(x_0, y) = u_{Bl}(y), \quad v_B(x_0, y) = v_{Bl}(y), \quad \omega_{z_B}(x_0, y) = \omega_{z_{Bl}}(y). \tag{6a–c}$$

At the wall, we use

$$u_B(x,0) = 0, \quad v_B(x,0) = 0, \quad \left.\frac{\partial v_B}{\partial y}\right|_{x,0} = 0, \tag{7a–c}$$

while the vorticity is calculated from

$$\left.\frac{\partial \omega_{z_B}}{\partial x}\right|_{x,0} = -\left.\frac{\partial^2 v_B}{\partial y^2}\right|_{x,0}. \tag{7d}$$

Equation (7*c*) is obtained from the continuity equation, while (7*d*) results from (5*b*). At the outflow boundary ($x = x_N$), we employ

$$\left.\frac{1}{Re}\frac{\partial^2 \omega_{z_B}}{\partial x^2}\right|_{x_N,y} = 0 \quad \text{and} \quad \left.\frac{1}{Re}\frac{\partial^2 v_B}{\partial x^2}\right|_{x_N,y} = 0, \tag{8a, b}$$

which then allows solution of the governing equations (5*a*) and (5*b*) at $x = x_N$, whereby u_B at $x = x_N$ is calculated from

$$\left.\frac{\partial^2 u_B}{\partial y^2}\right|_{x_N,y} = \left.\frac{\partial \omega_{z_B}}{\partial y}\right|_{x_N,y}. \tag{8c}$$

In our model, the free-stream boundary ($y = y_M$) is assumed to be far enough away from the wall so that the flow can be considered irrotational along this boundary. Thus we can assume

$$\omega_{z_B}(x, y_M) = 0. \tag{9a}$$

Then the free-stream velocity is prescribed according to a flat-plate boundary layer with zero pressure gradient

$$u_B(x, y_M) = 1. \tag{9b}$$

For the calculation of v_B, a von-Neumann-type gradient condition is used,

$$\left.\frac{\partial v_B}{\partial y}\right|_{x,y_M} = -\left.\frac{\mathrm{d}u_B}{\mathrm{d}x}\right|_{x,y_M} = 0, \tag{9c}$$

which is obtained from the continuity equation.

2.2. *Calculation of the unsteady disturbance flow*

2.2.1. *Governing equations*

As for the base flow, the governing equations for the calculation of the disturbance flow are based on the Navier–Stokes equations in a vorticity–velocity formulation written in a 'conservative' form with three vorticity transport equations for the three vorticity components $\omega'_x, \omega'_y, \omega'_z$,

$$\frac{\partial \omega'_x}{\partial t} + \frac{\partial}{\partial y}(v'\omega'_x - u'\omega'_y + v_B\omega'_x - u_B\omega'_y) - \frac{\partial}{\partial z}(u'\omega'_z - w'\omega'_x + u_B\omega'_z - u'\omega_{z_B}) = \tilde{\Delta}\omega'_x, \tag{10a}$$

$$\frac{\partial \omega'_y}{\partial t} + \frac{\partial}{\partial x}(v'\omega'_x - u'\omega'_y + v_B\omega'_x - u_B\omega'_y) + \frac{\partial}{\partial z}(w'\omega'_y - v'\omega'_z - v_B\omega'_z - v'\omega_{z_B}) = \tilde{\Delta}\omega'_y, \tag{10b}$$

$$\frac{\partial \omega'_z}{\partial t} + \frac{\partial}{\partial x}(u'\omega'_z - w'\omega'_x + u_B\omega'_z + u'\omega_{z_B}) - \frac{\partial}{\partial y}(w'\omega'_y - v'\omega'_z - v_B\omega'_z - v'\omega_{z_B}) = \tilde{\Delta}\omega'_z, \tag{10c}$$

and three Poisson-type equations for the velocity components u', v', and w',

$$\frac{\partial^2 u'}{\partial x^2}+\frac{\partial^2 u'}{\partial z^2}=-\frac{\partial \omega'_y}{\partial z}-\frac{\partial^2 v'}{\partial x\,\partial y}, \tag{10d}$$

$$\tilde{\Delta} v'=\frac{\partial \omega'_x}{\partial z}-\frac{\partial \omega'_z}{\partial x}, \tag{10e}$$

$$\frac{\partial^2 w'}{\partial x^2}+\frac{\partial^2 w'}{\partial z^2}=\frac{\partial \omega'_y}{\partial x}-\frac{\partial^2 v'}{\partial y\,\partial z}, \tag{10f}$$

where the Laplacian $\tilde{\Delta}$ in (10*a*), (10*b*), (10*c*), and (10*e*) is defined as

$$\tilde{\Delta}=\frac{1}{Re}\frac{\partial^2}{\partial x^2}+\frac{\partial^2}{\partial y^2}+\frac{1}{Re}\frac{\partial^2}{\partial z^2}. \tag{10g}$$

2.2.2. *Computational domain*

The governing equations (10) are solved within the computational box shown schematically in figure 1. For simulations of transition induced by a local disturbance source (such as a vibrating-ribbon-induced transition; see Klebanoff *et al.* 1962 and Kachanov *et al.* 1977), the inflow boundary may be upstream of the wavemaker. Thus, the computational domain includes the generation of the disturbance wave. However, instead of simulating a vibrating ribbon in our simulations, the disturbances are introduced by periodic blowing and suction through the wall within a narrow strip. From numerical simulations (Konzelmann, Rist & Fasel 1987) we have learned that this technique is very efficient with respect to generating 'pure' vorticity waves (without excessive acoustic contamination).

The downstream extent of the computational domain is assumed to be large enough so that the main wave front of the propagating disturbance waves does not reach the outflow boundary during the course of the computation. In the spanwise direction, the disturbance flow field is assumed to be periodic. Therefore, the spanwise extent of the domain is composed of one or more wavelengths of the disturbance flow.

2.2.3. *Boundary conditions*

Equations (10) are solved within the computational domain discussed previously. For the boundary conditions *at the wall* ($y=0$), we use no-slip conditions, thus

$$u'(x,0,z,t)=0, \quad w'(x,0,z,t)=0. \tag{11a, b}$$

The v'-velocity component is prescribed as a function of x, z, and t,

$$v'(x,0,z,t)=f'_v(x,z,t). \tag{11c}$$

This allows the generation of disturbances in the integration domain by local time-dependent blowing and suction within a narrow strip at the wall. This blowing and suction method is an alternative to the vibrating-ribbon technique in producing Tollmien–Schlichting waves (e.g. Kozlov & Levchenko 1987). Kozlov & Levchenko have compared both techniques and observed only a slight advantage of the 'classical' vibrating-ribbon technique over 'wall techniques' when employed in the laboratory. However, for numerical simulations, the blowing and suction technique can be implemented much more easily! With a given frequency and spanwise wavelength, different kinds of two-dimensional and pairs of three-dimensional oblique Tollmien–

Schlichting waves, as well as longitudinal vortices, can be generated. For the investigations discussed in this paper, we chose

$$f_v'(x,z,t) = A_{2D}\,Re^{1/2}\,v_a(x)\sin(\beta t) + A_{3D}\,Re^{1/2}\,v_s(x)\cos(\gamma z), \tag{12}$$

where A_{2D} denotes the amplitude and β the frequency of the two-dimensional disturbance input. The second term on the right-hand side of (12) generates longitudinal vortices and thus is simulating the effects of the pieces of scotch tape under the vibrating ribbon in the experiments of Kachanov *et al.* (1984, 1985). The amplitudes of the longitudinal vortices are controlled by the parameter A_{3D}, and the spanwise spacing is controlled by the wavenumber γ. The distributions of $v_a(x)$ and $v_s(x)$ in (12) used in the present calculations are shown in figure 1(*b*).

The vorticity components are calculated from the following equations:

$$\frac{\partial^2\omega_x'}{\partial x^2} + \frac{\partial^2\omega_x'}{\partial z^2} = -\frac{\partial^2\omega_y'}{\partial x\,\partial y} + \frac{\partial}{\partial z}\tilde{\Delta}v', \tag{13}$$

$$\omega_y'(x,0,z,t) = 0, \tag{14}$$

and

$$\frac{\partial\omega_z'}{\partial x} = \frac{\partial\omega_x'}{\partial z} - \tilde{\Delta}v'. \tag{15}$$

The *outflow boundary* is assumed to be downstream of the disturbance wave front. The disturbances can thus be assumed to be very small near the boundary and therefore follow a linear stability theory behaviour. Hence, at the outflow boundary, (10) are solved using

$$\left.\frac{\partial^2 f'}{\partial x^2}\right|_{x_N,\,y,\,z,\,t} = -\alpha^2 f'(x_N,y,z,t) \tag{16}$$

for all disturbance variables f', where $f' = (u', v', w', \omega_x', \omega_y', \omega_z')$. Equation (16) results from the assumption of neutral behaviour of the disturbance waves at this boundary. The wavenumber α is an expected wavenumber for the disturbances (near the outflow boundary) resulting from the primary instability (see Fasel, Rist & Konzelmann 1991).

Along the *free-stream boundary*, as for the base flow, we assume that this boundary is far enough from the wall so that potential flow can be assumed. Thus,

$$\omega_x'(x,y_M,z,t) = 0, \quad \omega_y'(x,y_M,z,t) = 0, \quad \omega_z'(x,y_M,z,t) = 0. \tag{17a–c}$$

For the v'-component, exponential decay in the y-direction is prescribed,

$$\left.\frac{\partial v'}{\partial y}\right|_{x,\,y_M,\,z,\,t} = -\frac{\alpha^*}{Re^{1/2}}v'(x,y_M,z,t), \tag{17d}$$

where α^* is an expected wavenumber dependent on x.

For the spanwise boundaries at $z=0$ and $z=\lambda_z$, periodicity conditions are employed. Thus, for all variables and their derivatives,

$$f'(x,y,0,t) = f'(x,y,\lambda_z,t), \tag{18a}$$

$$\left.\frac{\partial^n f'}{\partial z^n}\right|_{x,\,y,\,0,\,t} = \left.\frac{\partial^n f'}{\partial z^n}\right|_{x,\,y,\,\lambda_z,\,t}; \quad n = 1,2,\ldots \tag{18b}$$

are enforced.

When the disturbances are generated through the blowing and suction strip, as in the present investigation, the *inflow boundary* is moved far enough upstream of the strip so that the effect of the blowing and suction is negligible near the inflow boundary. Thus, we assume that all disturbances are zero at the inflow boundary,

$$f'(x_0, y, z, t) = 0, \tag{19}$$

where f' stands for the variables u', v', w', ω'_x, ω'_y and ω'_z, respectively.

3. Numerical method

Exploiting the periodicity conditions in the spanwise direction, a spectral ansatz can be introduced for all variables f':

$$f'(x,y,z,t) = \sum_{k=-K}^{K} F_k(x,y,t)\,\mathrm{e}^{\mathrm{i}k\gamma z}. \tag{20}$$

The wavenumber γ is related to the spanwise wavelength by $\gamma = 2\pi/\lambda_z$. The F_K are the complex conjugates of the F_{-k} and, therefore, governing equations (10) and boundary conditions (11)–(19) can be transformed into $K+1$ equations and boundary conditions for an (x,y)-plane integration domain.

Since the disturbance flow development that we intend to calculate is not only periodic with respect to the spanwise direction z but is also symmetric with respect to $z = 0, \pm\lambda_z/2, \pm\lambda_z, \ldots$, etc. the F_K for u', v' and ω'_z are all real, while the F_K for w', ω'_x and ω'_y are purely imaginary. Therefore, our numerical method does not require any complex arithmetic and requires only half the memory of a fully complex representation. Except for the first derivatives, all other derivatives with respect to x and y in the transformed (plane) equations and in the boundary conditions are discretized with finite differences of fourth-order accuracy. The finite-difference approximations used to discretize the first and second spatial (x-, y-) derivatives of the flow variables are given in the Appendix. The first derivatives are approximated with finite differences of eighth-order accuracy. Test calculations have shown that the use of these higher-order approximations for the first derivatives improves the numerical stability of the method. We observed that grid-scale oscillations in the x-direction occurred before the method failed to converge. These oscillations were avoided either by using a smaller step size without changing the order of the discretization or by increasing the order of the central differences without changing the step size. In the meantime we learned that higher-order central differences (smaller aliasing errors) approximate small wavelengths better than lower-order finite differences and that grid-scale oscillations are due to an unphysical amplification of not well-resolved wave components (caused by the time integration scheme). Similar observations most probably led to the use of upwind-biased differences by Rai & Moin (1991, 1993).

For time integration of the vorticity transport equations (10*a*–*c*), an explicit Adams–Bashforth procedure of third-order accuracy is employed,

$$\Omega_k^{l+1} = \Omega_k^l + \frac{\Delta t}{12}(23\mathrm{R}_k^{l-1} - 16\mathrm{R}_k^{l-2} + 5\mathrm{R}_k^{l-3}), \tag{21}$$

where Ω_k denotes Ω_{x_k}, Ω_{y_k}, and Ω_{z_k}; R_k denotes the right-hand sides of the discretized vorticity transport equations; and l denotes the time level. The present numerical method represents a significant improvement over our previous method with respect to computational efficiency. With our new method, comparable simulations require only one-tenth the computation time of our previous implicit method (Fasel *et al.* 1990). The reason for this considerable reduction in computation time is twofold. First, the explicit Navier–Stokes method allows considerably better adaptation to and exploitation of the vector architecture of the CRAY-2 supercomputer used for these simulations. Secondly, the explicit third-order-accurate Adams–Bashforth method has relatively good numerical stability characteristics, so in order to assure numerical stability, the time step Δt in our present simulation needed to be reduced only to one-sixth of the Δt used in the implicit calculations. For details concerning the numerical method, see Rist (1990).

4. Numerical results

Based on the numerical method discussed above, a computer code was developed to solve the governing equations together with the boundary and initial conditions as specified in the previous section. However, before employing this code for the investigation of complicated nonlinear transition phenomena, such as the fundamental breakdown which is considered in this paper, numerous test calculations were performed to check the validity of the code for transition simulations.

4.1. *Code validation*

We performed test calculations with very small two- and three-dimensional disturbance waves. This allowed detailed comparison with linear stability theory and thus enabled a thorough check of the performance of the computer code and the numerical method upon which the computer code is based. Of the many linear test calculations performed, owing to lack of space here we will only present the results of two typical calculations.

In addition to small-amplitude calculations, the code was also subjected to more complex situations, where the effect of nonlinearities became important. For example, we performed comparison calculations using the experiments of Kachanov & Levchenko (1984) for a subharmonic breakdown. Subharmonic breakdown can be captured accurately by secondary instability theory and, therefore, the numerical method could be scrutinized by using both experimental measurements and theoretical results for comparison with the numerical results.

4.1.1. *Linear test calculations*

Results of linear test calculations are given here for a two-dimensional case $\gamma = 0$ and a three-dimensional case with $\gamma = 20$. The amplitude for the two-dimensional case was $A_{2D} = 10^{-5}$ and for the three-dimensional case $A_{3D} = 10^{-5}$, and the frequency was $\beta = 10$ (which corresponds to $F = (2\pi)\tilde{\beta}(\tilde{\nu}/\tilde{U}_{\infty}^{2}) \times 10^{4} = 1.0$). The three-dimensional disturbances are generated analogously to the two-dimensional disturbances by timewise periodic suction and blowing, i.e. $A_{3D}\,Re^{1/2}\,v_a(x)\sin(\beta t)\cos(\gamma z)$ instead of $A_{3D}\,Re^{1/2}\,v_s(x)\cos(\gamma z)$ as in equation (12). Typical results of these linear calculations are shown in figures 2 and 3 and are compared with linear stability theory. In figure 2, for these two cases, the amplification rates of the Navier–Stokes calculations as obtained for the maxima of the u', v', and w' disturbance profiles are compared with the amplification rates obtained from linear theory (in figure 2, please note the location of the disturbance strip; also, for clarity, the three-dimensional amplitude waves are shifted in the y-direction relative to the two-dimensional amplification waves). For the u'_{max} criterion, the curves agree very well with those of linear stability theory. The observed deviations, in particular for the v'_{max} and w'_{max} criteria, are well within the differences that can be accounted for by the so-called 'non-parallel' effects (see Gaster 1974 and Fasel & Konzelmann 1990). Comparison of the amplitude distributions for

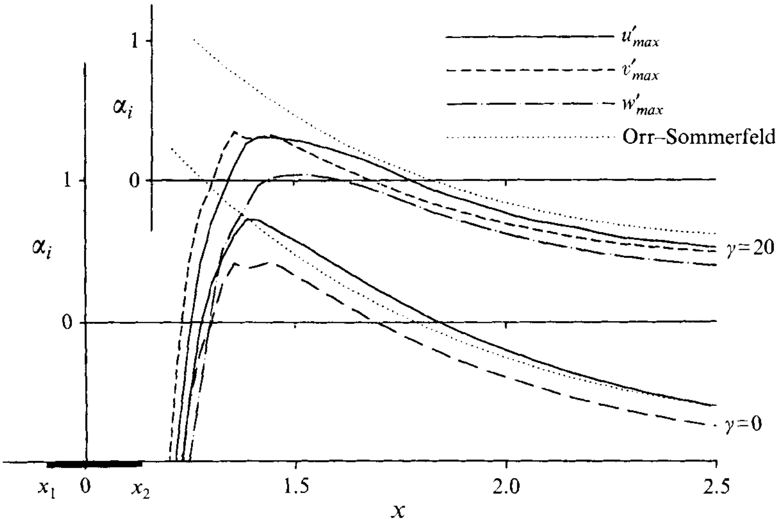

FIGURE 2. Comparison of amplification rates of the Navier–Stokes calculations with linear stability theory for two-dimensional ($\gamma = 0$) and three-dimensional waves ($\gamma = 20$).

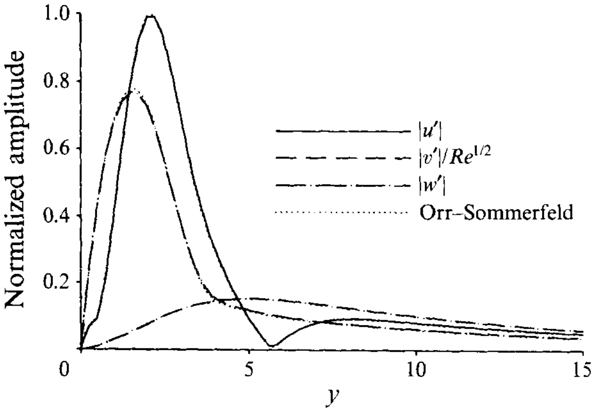

FIGURE 3. Comparison of the amplitude distributions of the Navier–Stokes calculations with linear stability theory. $x = 2.0$, $\beta = 10$, $\gamma = 20$.

the three-dimensional calculations ('eigenfunctions') is shown in figure 3. The agreement is so good that the corresponding curves practically coincide with each other.

4.1.2. *Subharmonic breakdown*

To check the suitability of the numerical code for investigating nonlinear transition phenomena, test calculations were performed for a subharmonic breakdown. Detailed experimental data for this case, which can be used for comparison with our Navier–Stokes results, are available from the laboratory experiments by Kachanov & Levchenko (1984). Therefore, for this test calculation, the parameters were chosen so that the conditions in the experiments were matched as closely as possible. The results of the Navier–Stokes calculations agreed extremely well with the experiments. In general, the quantitative agreement between numerical results and experiments was at least as good or even better than that achieved with our previous Navier–Stokes code (see Fasel *et al.* 1990).

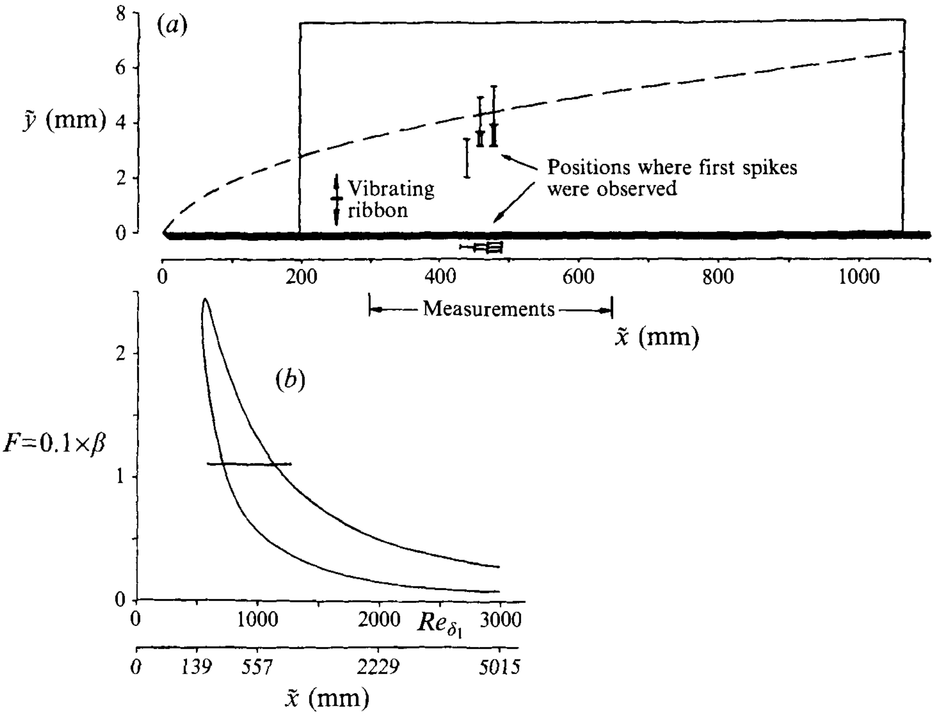

FIGURE 4. Position of the computational domain: (*a*) relative to the experiments by Kachanov *et al.* (1984, 1985); (*b*) relative to the stability diagram of linear stability theory.

The numerical method presented in this paper could still be improved in a number of ways, e.g. by the use of a different outflow boundary treatment (cf. Kloker *et al.* 1993) which in turn would allow the use of more spanwise Fourier modes, and hence better resolution in z. However, the present simulations with a relatively coarse grid are interesting in many ways. Our results show that only few spanwise modes are necessary to compute the essential physics. This observation may have implications for future large eddy and direct numerical simulations of transition to turbulence.

4.2. *Numerical simulations of the fundamental breakdown experiments by Kachanov et al.* (*1984, 1985*)

Kachanov *et al.* (1984) intended to repeat the experiments of Klebanoff *et al.* (1962) in order to better understand the three-dimensional transition phenomena and to reveal the relevant mechanisms for this type of breakdown, which was later classified as 'fundamental breakdown' (or K-type breakdown). For our numerical simulations, all parameters were chosen such that the set-up of the experimental investigations of Kachanov *et al.* (1984) could be modelled as closely as possible. In figure 4, the computational domain for these simulations is shown in the laboratory frame of reference of the experiments by Kachanov *et al.*

Figure 4 also shows the location of the vibrating ribbon ($\tilde{x} = 250$ mm), as well as the approximate locations where the characteristic 'spikes'† occurred. As also indicated in figure 4, the measurements in the experiments were taken between $\tilde{x} = 300$ and 650 mm. The free-stream velocity was $\tilde{U}_\infty = 9.18 \text{ m s}^{-1}$ and the frequency of the

---

† This term describes short-time, large-amplitude changes of the u'-velocity signals *vs.* time, first observed in experiments by Klebanoff *et al.* (1962).

vibrating ribbon was $\tilde{\beta} = 96.4\,\text{Hz}$. For our calculations, the inflow boundary was located at $\tilde{x}_0 \approx 190\,\text{mm}$ and the outflow boundary was moved downstream (as discussed in §3) until $\tilde{x}_N \approx 1050\,\text{mm}$ was reached. The Reynolds number used in equations (1)–(17) was $Re^* = 100000$, with $\tilde{\nu} = 1.51 \times 10^6\,\text{m}^2\,\text{s}^{-1}$ (kinematic viscosity of air). This leads to a reference length $\tilde{L} = 165\,\text{mm}$. Thus the Reynolds number based on displacement thickness, defined as $Re^* = 1.72078(x\,Re)^{1/2}$ for the inflow boundary, is $Re^* = 580$ and for the final location of the outflow boundary $Re^* = 1375$. In the y-direction, the computational domain extends for 8 (inflow) displacement thicknesses. Test calculations have shown that 8 displacement thicknesses are sufficient. For example, a calculation with 12 displacement thicknesses showed practically no differences in the results up to $\tilde{x} = 450\,\text{mm}$ (Rist 1990). The validity of the far-field boundary condition may also be checked by comparison of the numerical results with the experimental measurements. In a simulation of the later stages, however, when vorticity fluctuations (especially at peak) reach the upper boundary, the boundary is too close to the wall with only 8 displacement thicknesses distance. This can be observed in the results further down, but as it appears at an x-station downstream from the station where the spanwise resolution is insufficient, and as the comparisons with the experiments show no upstream influence, the results are not affected by the far-field boundary.

In the simulations, the disturbance input was at approximately the same downstream location as in the experiments. However, instead of simulating the disturbance generation by a vibrating ribbon, the disturbances in the simulations were generated by blowing and suction within a narrow strip as discussed in §2.2.3. With the reference velocity $\tilde{U}_\infty$ and the reference length $\tilde{L}$, the dimensionless frequency given by $\beta = (2\pi)\tilde{\beta}\tilde{L}/\tilde{U}_\infty$ was $\beta \approx 11$, and the dimensionless frequency parameter $F = (\beta/Re) \times 10^4 = 1.1$. In the experiments of Kachanov *et al.*, the three-dimensionality of the disturbances was introduced by using strips of scotch tape that were glued onto the flat plate directly under the vibrating ribbon. The distance of these spacers was 12.5 mm and therefore the spanwise wavelength was 25 mm. This results in a non-dimensional spanwise wavenumber $\gamma = \tilde{\gamma}\tilde{L} = 41.5$. The streamwise wavenumber, α, required for the outflow conditions (16) was obtained from linear theory and, thus, $\alpha = 30$ was used. The wavenumber α^* required in equation (17*d*) for each spanwise harmonic was calculated from the relation $\alpha^{*2} = \alpha^2 + (k\gamma)^2$. The number of spanwise Fourier modes was set to 17 (i.e. $K = 8$ in (20)) for the solution of the governing equations, and to 32 for the alias-free computation of the nonlinear terms in (10).

For the present simulations, the base flow was calculated using 65 grid points in the y-direction and 3000 grid points in the x-direction. As discussed below, the downstream extent of the computational domain for the calculation of the disturbance flow increases during the course of the actual simulations as the outflow boundary is moved downstream in order to stay clear of the leading edge of the disturbance's wave front. Therefore, the number of grid points used in the x-direction was $N = 658$ at the beginning of the unsteady calculation. N was increased by 184 at the beginning of each new disturbance cycle. Thus, 2498 grid points in the x-direction were used when the simulation was stopped after 11 disturbance cycles.

The time direction was discretized such that one period of the fundamental disturbance cycle was initially divided into 1200 intervals, Δt. This was determined from stability considerations to ensure numerical stability of the explicit Adams–Bashforth time integration scheme as discussed in §3. Also for stability reasons, after seven disturbance cycles, the number of time intervals per period had to be increased

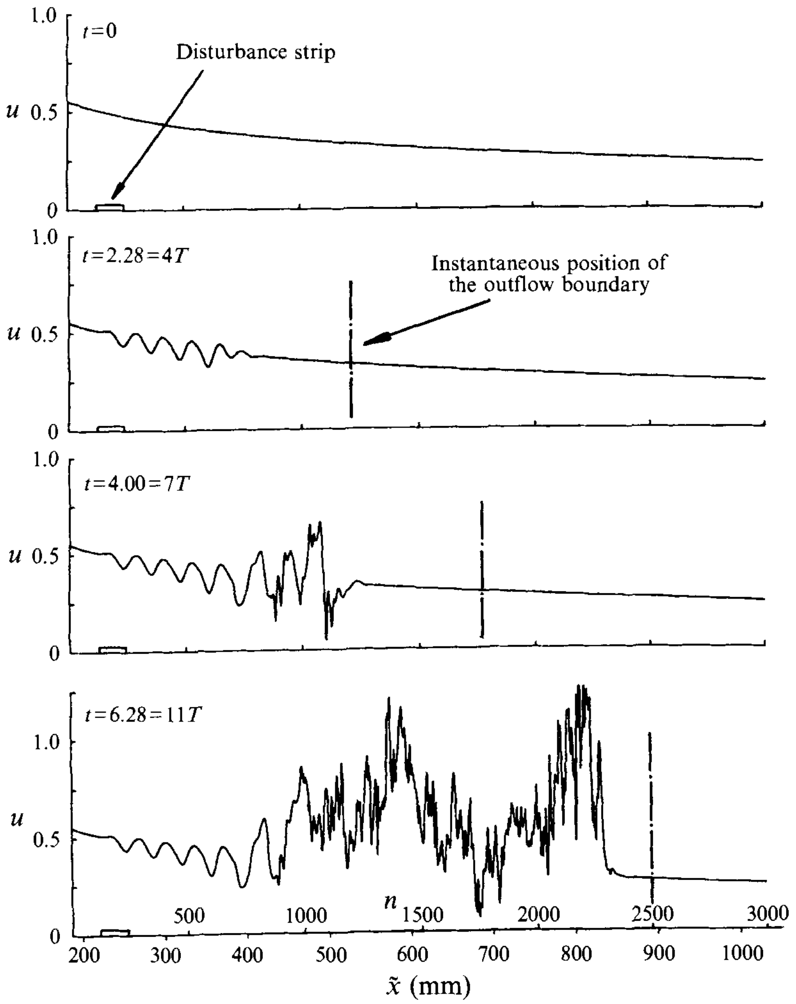

FIGURE 5. Instantaneous u-velocity component at $z = 0$ and $\tilde{y} = 0.95$ mm for four different time instants.

from 1200 to 1680 because the maximum instantaneous velocity increases due to the influence of the nonlinear disturbances and therefore the initially satisfied CFL criterion is violated unless the time step is reduced. There is actually no danger in calculating with a too big time step, and thus producing spurious results, since the simulation will 'blow up' within a few time steps when the CFL criterion is violated. The simulation was carried out using the CRAY-2 supercomputer at the University of Stuttgart and required approximately 46 h of CPU time and 96 megawords of memory. During the simulation, up to 14.7 gigawords of numerical data per primary disturbance cycle had to be calculated. For the results presented here, only 1 gigabyte of data for the eleventh calculated time period could be stored on disk and then used as a database for detailed comparisons with the experiments.

A typical response of the flow field subjected to the periodic disturbance input at the blowing and suction strip is shown in figure 5. For three different time instants, the instantaneous streamwise velocity component u for a constant $\tilde{y} = 0.95$ mm (which is close to the u'-maximum of the two-dimensional Tollmien–Schlichting wave) and $z = 0$

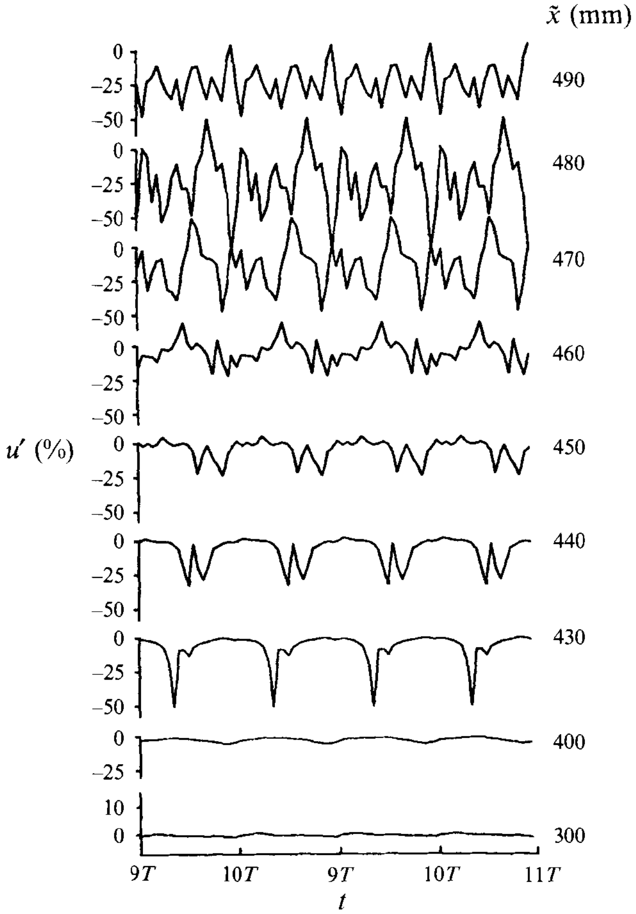

FIGURE 6. Time signals of the u'-disturbance velocity for different downstream locations and $\tilde{y} = 2.87$ mm, $z = 0$.

is plotted versus x. As the disturbance waves travel downstream, they assume an increasingly nonlinear character until at some downstream location, $\tilde{x} > 430$ mm, the first signs of randomness appear, which is about the location where spikes were observed in the experiments. Also indicated in figure 5 is the instantaneous location of the outflow boundary, which, as discussed earlier, is moving downstream as the calculation progresses. Beyond $\tilde{x} = 450$ mm, the flow is no longer periodic in time but rather exhibits a 'chaotic' or 'turbulent' behaviour. Of course, the number of grid points in the calculation is not sufficient to adequately resolve this 'turbulent' motion (although we believe it is sufficient to resolve the motion of the most energetic eddies and therefore the motion in this turbulent region qualitatively resembles that of a low Reynolds number turbulent boundary layer). However, the numerical resolution is sufficient to realistically model the early and intermediate transition stages up to the development of the spike stages which, as observed in experiments, just precede the actual breakdown to the random motion. In the regime of interest, i.e. upstream of the spike stages, the flow field is still periodic in time owing to the periodic disturbance generation. This allows detailed analysis of the data (using, for example, Fourier decomposition of the flow field) and enables detailed comparison with the experimental data. This periodicity of the time signals can be observed in figure 6, where the u'-

disturbance is plotted versus t at the peak station $z = 0$ and at a constant distance y from the wall. This is the distance from the wall where the spike in the time signal shows up strongest, which is clearly seen for $\tilde{x} = 430$ mm.

Figures 7 and 8 show direct comparisons between simulation and experiment for various Fourier components. The Fourier amplitudes of the Navier–Stokes solution and the corresponding phase relations for various wave components of the u disturbance velocity at the peak station are plotted in figure 7, together with corresponding experimental data. These amplitude and phase distributions are presented for various downstream x-locations starting from $\tilde{x} = 300$ mm up to $\tilde{x} = 430$ mm. The amplitude distributions of the various wave components from the Navier–Stokes calculations agree quite well with those from the experiments. Even for our last measuring station, $\tilde{x} = 430$ mm (figure 7*d*), there is still a good qualitative, and to some degree quantitative, agreement between simulation and experiment, although the resolution in the simulation can no longer be considered adequate. Moreover, even the comparison of the phase distribution between simulation and experiment shows good agreement, considering the difficulties in reliably determining phases from the experimental data (Kachanov *et al.* 1984, 1985). In particular, the numerical phase distribution also exhibits the characteristic phase synchronization for $\tilde{x} = 400$ mm (figure 7*c*) at between approximately 2 mm and 3 mm from the wall. Kachanov *et al.* identified this synchronization as being characteristic for the development of the spikes. Indeed, spikes in the time signals of the calculation do occur shortly downstream of this station, between 400 mm and 430 mm, and at a y-location above 2 mm, as seen in figure 6. This phase behaviour is even more pronounced in figure 7(*d*) for $\tilde{x} = 430$ mm, where the location of the synchronization has moved farther away from the wall to approximately 3.5 mm. At approximately this location in the experimental measurements, the velocity signal showed a spike that was also observed in our numerical simulation (figure 6).

Thus, our numerical simulations support the experimental observations that the occurrence of spikes is clearly associated with a phase synchronization of all wave components in a narrow y-range. Our results therefore lend support to the conjecture put forth by Kachanov *et al.* that the spike development should not be seen as a sudden 'new' event in the successive transition development, but rather that it is a consequence of the downstream development of the various wave components and their nonlinear interactions with each other. In other words, the sudden spike development should not be seen as an event decoupled from the upstream region; on the contrary, the contribution of the wave components to the spike generation may be traced upstream and therefore the spike development can be viewed as a predictable event.

The spanwise variation of the Fourier amplitudes of the various velocity wave components for a constant distance from the wall together with their respective phase relations are shown in figure 8 for different downstream locations. As seen from figure 8(*a*), for the first measuring station, $\tilde{x} = 300$ mm, there are still qualitative deviations between the simulation and experiments, in particular for the phases. This is likely to be due to the difficulty in our numerical simulations of exactly modelling the wave generation of the experiments. Therefore, the 'transient' downstream development in the vicinity of the location of the wave generation will be somewhat different in the numerical simulation unless the wave generation of the experiments can be modelled exactly. Based on the differences in the mean flow variation of u (Fourier component) between experiment and simulation, it appears that there is a much stronger spanwise modulation in the experimental measurements than in the simulation. This suggests that the tape strips glued onto the plate in the experiments may have led to a

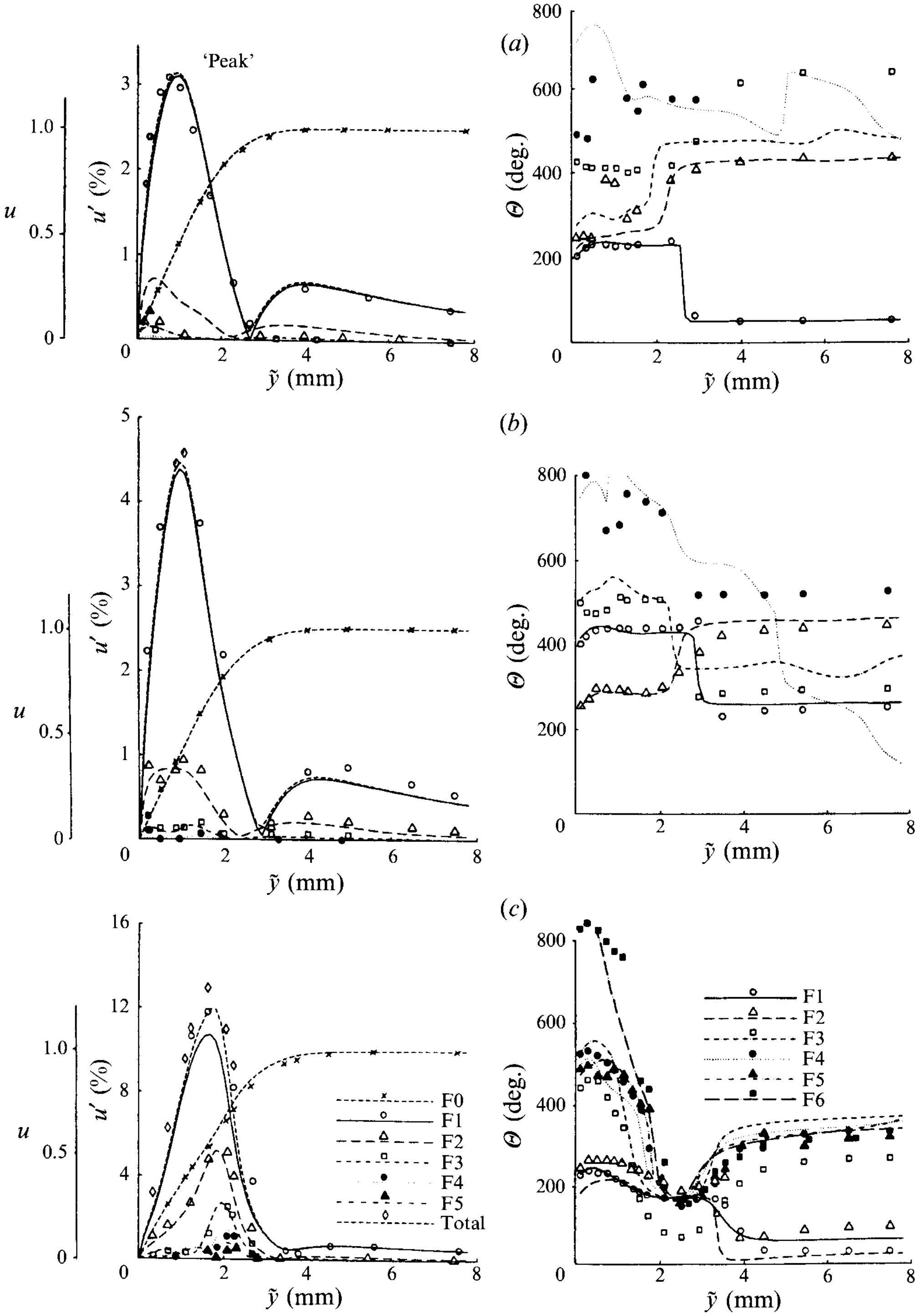

FIGURE 7(*a–c*). For caption see facing page.

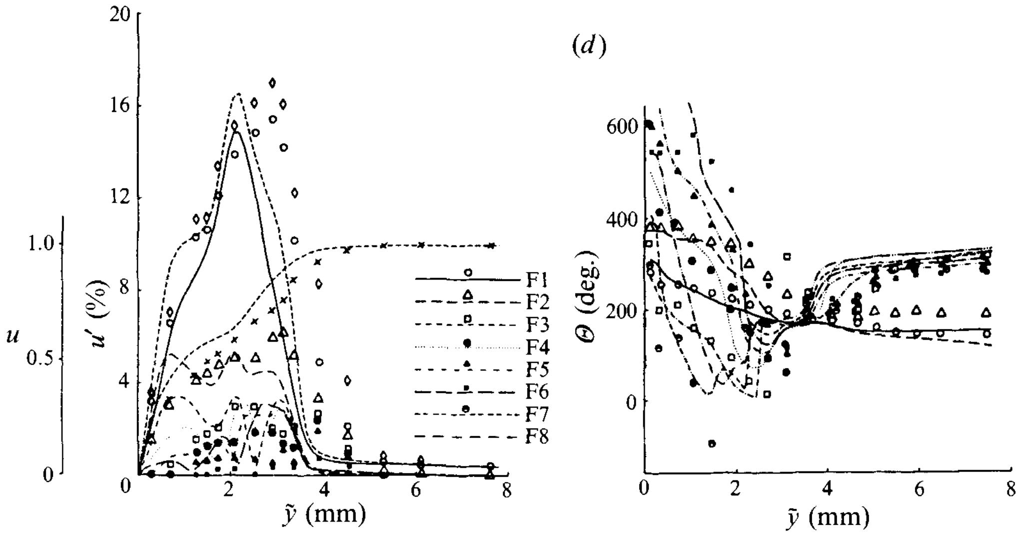

FIGURE 7. Comparison of amplitude and phase distributions at the peak station of the Navier–Stokes simulations (lines) with measurements by Kachanov *et al.* (1984, 1985) (symbols) for various downstream locations: (*a*) $\tilde{x} = 300$ mm; (*b*) $\tilde{x} = 350$ mm; (*c*) $\tilde{x} = 400$ mm; (*d*) $\tilde{x} = 430$ mm. F1, F2, etc. denote the frequencies of the fundamental wave, and its higher harmonics, respectively.

locally stronger mean flow variation than we had introduced with our disturbance generation according to equation (12). However, for the next measuring station, $\tilde{x} = 350$ mm in figure 8(*b*), the numerical and experimental mean flow variations are in better quantitative agreement, suggesting that the effect of different local 'transient' behaviours due to the difference in disturbance generation in the experiments and in the simulations has subsided. Nevertheless, certain consistent quantitative differences between experiments and simulations do persist and they may well be a consequence of these different disturbance generations. However, in the light of the otherwise excellent agreement of the amplitude distributions and phases, as discussed in connection with figure 7, this possible difference in the disturbance generation does not essentially alter the underlying physical mechanisms of the subsequent nonlinear behaviour. Also, it should be noted that the relatively small deviations between experimental and numerical data may also be due to experimental measuring uncertainties and other difficulties of performing such difficult experiments (see Kachanov *et al.* 1984).

For $\tilde{x} = 400$ and 430 mm in figures 8(*c*) and 8(*d*), the simulations nicely capture the strong spanwise modulation of the wave components. For $\tilde{x} = 430$ mm (figure 8*d*), the action is essentially concentrated within a very narrow spanwise range at the spike location where, as seen in figure 7(*d*), amplitudes can reach values of more than 16% of the mean flow! The large difference between the total r.m.s.-signal and the fundamental near the peak station is indicative of the large contribution of the higher harmonics to the spike, as initially observed by Kachanov *et al.* (1984).

It is obvious from figures 7 and 8 that additional wave components, other than the fundamental disturbances introduced at the disturbance strip, are present. These additional components must be generated locally as no other additional disturbances were introduced into the calculations. Thus, these additional components must be generated by the nonlinear terms in the Navier–Stokes equations, which enable nonlinear interactions of the two- and three-dimensional wave components. An

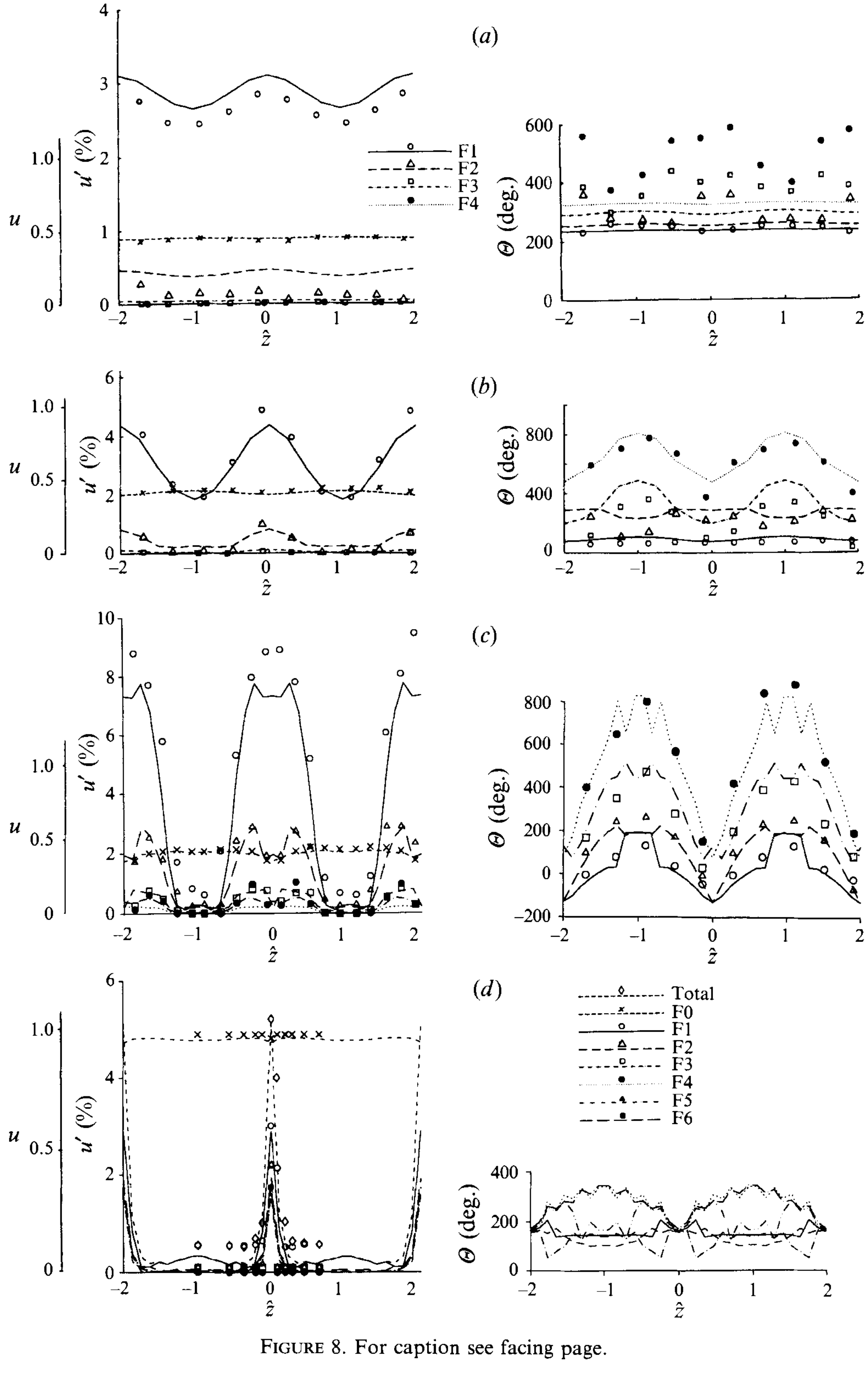

FIGURE 8. For caption see facing page.

excellent overall impression of the rapid generation of these additional wave components as the downstream distance increases can be obtained from figures 9 and 10. In figure 9, for the u-velocity disturbances, the Fourier amplitudes, $\hat{u}_{h,k}$, of the various spanwise and streamwise wave components are plotted in a perspective representation, where h denotes the multiple of the fundamental frequency and k denotes spanwise wave components according to

$$u'(x,y,z,t) = \sum_{h=0}^{H} \sum_{k=-K}^{K} \hat{u}_{h,k}(x,y)\cos[(h\beta_0 t + k\gamma z) - \Theta_{h,k}(x,y)]. \tag{22}$$

Figure 9(a), for $\tilde{x} = 247.5$ mm, which is near the end of the disturbance strip, demonstrates that, as intended, we are generating mainly a two-dimensional fundamental wave component (1,0) and, in addition, we introduce a very small spanwise periodic variation of the base flow in order to model the effect of the spacers used in the experiment. The two-dimensional disturbance amplitude is already large enough so that a small but recognizable two-dimensional first harmonic is generated, (2,0). At the next station, $\tilde{x} = 289$ mm, which is close to the first measuring station, the two-dimensional first harmonic has grown considerably relative to the fundamental (1,0) component, and a small two-dimensional second harmonic (3,0) appears. However, owing to the interaction of the two-dimensional fundamental component (1,0) with the three-dimensional stationary mode (0,1), the longitudinal vortices, three-dimensional fundamental components (1,1), (1, −1), are created. Initially, the effect of nonlinear interactions appears to be such that both spanwise (three-dimensional) and two-dimensional wave components are created with about equal priority (maybe with, at first, a slight bias towards generating two-dimensional components). Beyond $\tilde{x} = 330$ mm (see figure 9c), it is apparent, however, that spanwise components are generated at a much more rapid rate than two-dimensional components. This can be seen from the fact that the amplitude spectra in figure 9 are spreading much more rapidly in the k-direction than in the h-direction. Comparing the spectra for two consecutive downstream stations, it is obvious that this process is rapidly accelerating. This is particularly apparent when comparing $\tilde{x} = 371$ mm, which is still upstream of the first spike stage, and figure 9(e) for $\tilde{x} = 412.5$ mm, which is at about the first spike stage. With increasing spanwise wavenumber and frequency the amplitudes of the modes decrease. One exception is at the last station, $\tilde{x} = 413$ mm (in figure 9e), where the amplitudes increase again at the spanwise boundary of the spectrum (compare curves $k = 7$ and $k = 8$). This increase is due to an insufficient number of Fourier modes in equation (20), but not due to aliasing since the computation of the nonlinear terms has been de-aliased by the 2/3-rule.

The rapid downstream growth of the spanwise wave components is even better displayed in figure 10 where Fourier amplitudes of the various spanwise spectral components for the fundamental frequency $(1,k)$ are plotted versus the downstream coordinate x. For comparison, the three-dimensional steady mode (0,1) and the mean-flow distortion relative to the base flow [mode (0,0)] are also shown. In particular, figure 10 also shows clearly that the higher k modes enter at an increasingly faster rate as x increases and the growth rate of the next k mode is initially larger than the

---

FIGURE 8. Amplitudes and phases versus $\tilde{z} = \gamma z/\pi$ for a constant distance from the wall and for various downstream locations: (a) $\tilde{x} = 300$ mm, $\tilde{y} = 0.97$ mm; (b) $\tilde{x} = 350$ mm, $\tilde{y} = 0.96$ mm; (c) $\tilde{x} = 400$ mm, $\tilde{y} = 0.96$ mm; (d) $\tilde{x} = 430$ mm, $\tilde{y} = 3.47$ mm (experiment: $\tilde{y} = 4.5$ mm). Lines are results from calculations; symbols are measurements from Kachanov *et al.* (1984, 1985). F1, F2, etc. denote the frequencies of the fundamental wave, and its higher harmonics, respectively.

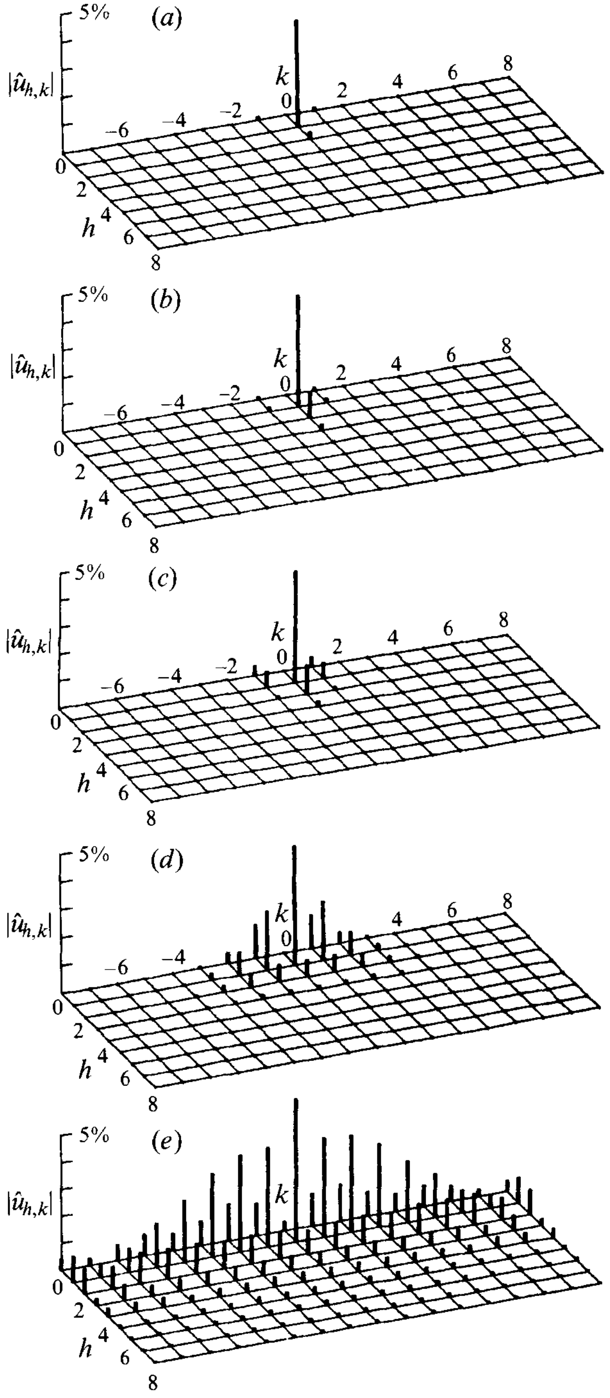

FIGURE 9. y-maxima of the Fourier amplitudes of the disturbance wave components as a function of spanwise and streamwise wavenumber, in perspective view. (*a*) $\tilde{x} = 248$ mm, (*b*) $\tilde{x} = 289$ mm, (*c*) $\tilde{x} = 330$ mm, (*d*) 371 mm, (*e*) $\tilde{x} = 413$ mm.

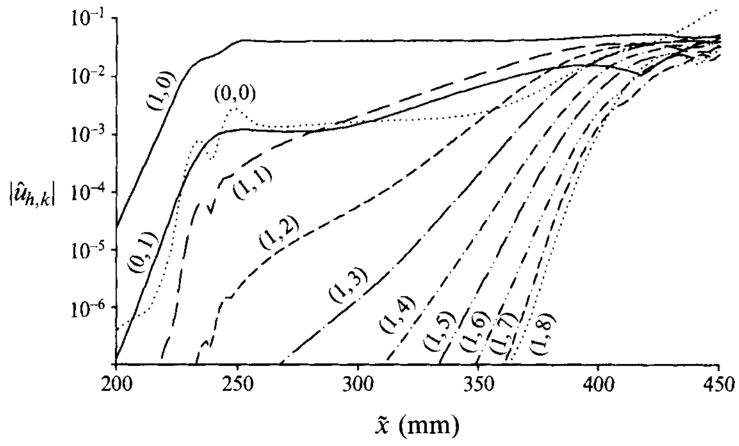

FIGURE 10. Development of the y-maxima of the Fourier amplitudes in the downstream direction of selected modes of figure 9.

preceding $k-1$ mode. Also, all the modes appear to saturate beyond $\tilde{x} = 420$ mm, where they reach the same order of magnitude in amplitude. One exception is the highest spanwise mode, $k = 8$, which has already started to increase above $(1,7)$ at $\tilde{x} = 400$ mm. It is important to note that a simultaneous increase of other modes (e.g. $(1,6)$ and $(1,7)$) does not occur; they are apparently not strongly affected by the increase of the eighth spanwise mode. This may explain why the present results compare so well with the experiment downstream of $\tilde{x} = 400$ mm.

The rapid spreading of the spanwise wavenumber spectrum is consistent with the findings of Klebanoff *et al.* (1962), who suggested that the three-dimensional development strongly dominated the two-dimensional development after the two-dimensional waves had reached a certain amplitude and that therefore the three-dimensional development was crucial to the breakdown process. This strong three-dimensional behaviour in a sense motivated Klebanoff *et al.* to trigger the three-dimensional development by introducing controlled three-dimensional wave components using spacers under the vibrating ribbon. However, based on the results of our simulation, we conjecture that compared to Kachanov *et al.*'s experiment, the two-dimensional wave amplitude was initially only half as large as in the Kachanov *et al.* experiments. This may be due to the different experimental conditions at the location of the vibrating ribbon (local Reynolds number, amplitude, and frequency) in generating the two- and three-dimensional waves. In the experiments by Klebanoff *et al.*, the three-dimensional components were thus larger relative to the two-dimensional components right from the outset of the disturbance generation than in the experiments by Kachanov *et al.* This is consistent with Klebanoff *et al.*'s statements that in their experiments two-dimensional wave development was negligible and that higher harmonics of the two-dimensional wave components were unimportant. Kachanov *et al.*, on the other hand, observed and measured sizable two-dimensional higher harmonic wave components and therefore disagreed with Klebanoff *et al.* and stated that two-dimensional higher harmonics do play an important role in the breakdown process. Our calculations support the measurements of Kachanov *et al.*; in fact, we also observed significant higher-harmonic two-dimensional wave components (see figure 9*a–e*). However, we disagree with Kachanov's (1987) interpretation that Klebanoff *et al.* underestimated the role of the higher harmonics. As mentioned earlier,

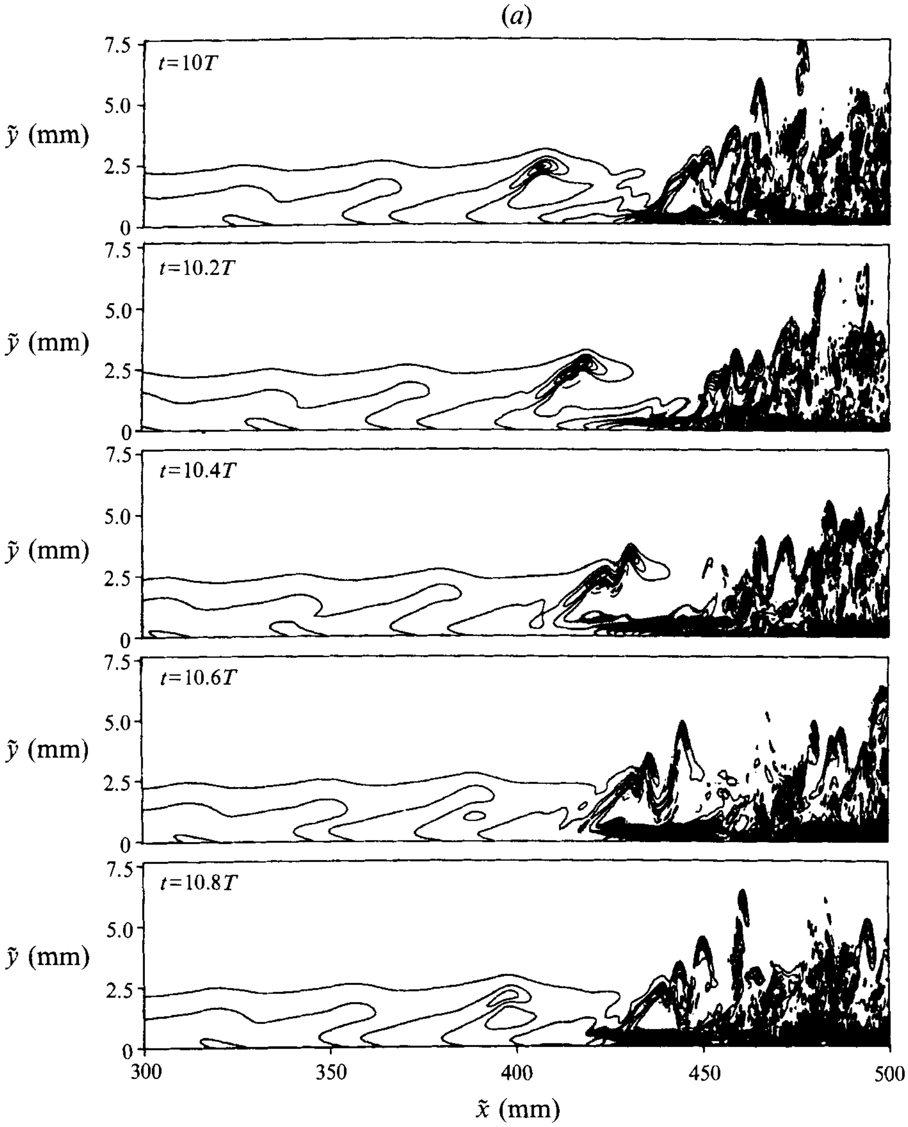

FIGURE 11 (*a*). For caption see facing page.

in our opinion the discrepancy is probably due to differences in the disturbance generation, in particular with respect to the (relative) amplitudes of the two- and three-dimensional wave components. In spite of the differences in the disturbance generation, it appears however that the fundamental mechanisms responsible for the three-dimensional breakdown are very similar for both experiments.

In the light of the results discussed so far, in particular the close agreement with the experiments, we feel confident that with our numerical model we can reliably simulate the transition process in the experiments by Kachanov *et al.* (1984, 1985). It should be mentioned that in contrast to earlier simulations (using the temporal model) our simulation results show the true spatial development of the disturbances, and are hence qualitatively and quantitatively much closer to the experiment. In particular, there is no ambiguity regarding the velocity needed for the transformation of temporal results

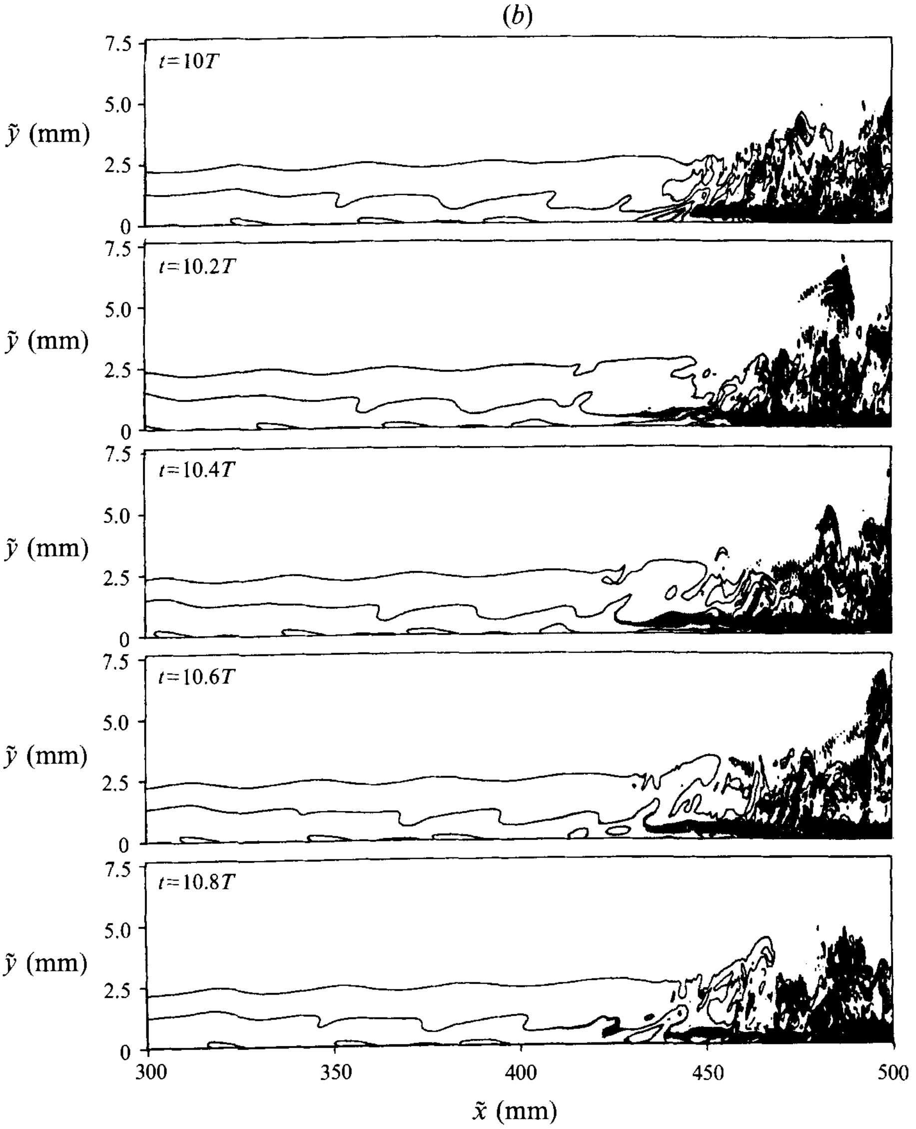

FIGURE 11. Instantaneous isolines for the spanwise vorticity component ω_z at planes z = const. for several time instants during a Tollmien–Schlichting period: (*a*) peak plane, $z = 0$; (*b*) valley plane, $\tilde{z} = 12.5$ mm.

into spatial results. Therefore, we feel we can use our simulations to extract information from the numerical data that cannot (or only under considerable difficulties) be obtained from the experimental data. From our simulations, we have available instantaneous data using an extremely fine spatial and temporal mesh. Also, the data are 'clean', that is they are uncontaminated by the effects of intrusive probes or of free-stream turbulence or other influencing factors in the experiments.

Of great interest, for example, is an investigation of the development and behaviour of dominant vortical structures and an understanding of their importance in the transition process. Also of immediate interest would be the question of whether the dominant structures in the transition process *à la* Kachanov *et al.* (1985) are similar to those in the experiments of Williams, Fasel & Hama (1984) who made an attempt to identify structures and interpret their role in the transition process.

The dynamics of the flow field during the transition process are nicely demonstrated in figure 11, where contours of the instantaneous vorticity component ω_z are plotted for five representative time instances during one period of the fundamental Tollmien–Schlichting wave. The plots represent only part of the entire integration domain. In figure 11 (*a*), which is for a spanwise peak location ($z = 0$), we can observe the development of a localized maximum of ω_z vorticity (high-shear layer) which, while propagating downstream and moving away from the wall, becomes significantly deformed. Later, this vorticity concentration breaks up violently into smaller distinct vorticity lumps (we can clearly identify four), which are accelerating away from the wall. The spikes observed in the time velocity signals of the u'-component are directly linked to the birth of these small but obviously highly energetic vortices, as already shown by Kovasznay *et al.* (1962). Associated with (or caused by) this breakup of the vortical ω_z structure are concentrations of very high ω_z very close to the wall. In a movie that we produced from the simulation data, we could observe that every other vorticity lump that is generated in the breakdown of the high-shear layer moves towards the wall, where it merges with the region of high wall shear, while the other vorticity lumps generated by this breakup propagate away from the wall. In contrast, for the spanwise valley stations (figure 11 *b*), such localized ω_z concentrations away from the wall do not develop. Rather, we can observe the generation of large ω_z concentrations very close to the wall as for the peak stations (but farther downstream than where the breakup occurs in the peak station).

An overall impression of the shape of the vortical structures involved in the three-dimensional development prior to breakdown can be obtained from figure 12. In this figure, surfaces of constant spanwise (total) vorticity ω_z and constant longitudinal (total) vorticity ω_x are shown in perspective representation for two time instants, $t = 10T$ and $10.4T$. The structures in figure 12 may be compared qualitatively (e.g. Biringen 1987; Krist & Zang 1987). However, in contrast to the temporal simulation, here successive structures in the downstream direction are spatially apart, i.e. they do not overlap. This is an important qualitative difference to temporal simulations. It should be noted that the small-spanwise-scale longitudinal structures at $t = 10.4T$ are a consequence of spanwise grid-scale oscillations that are due to the overshoot of modes $k = 8$ at $\tilde{x} > 400$ mm, which were already observed in figures 9 and 10. The grid-scale oscillations are directly linked to the occurrence of large z-gradients near $z = 0$ and they move downstream with the flow structures to which they adhere. Thus, for constant x they repeatedly appear and disappear and there is no indication to suggest that the results become wrong with the first appearance of these oscillations. Rather, the main (physical) structures are still correct, at least qualitatively. The surfaces of constant ω_z (which is essentially $\partial u/\partial y$, as $\partial v/\partial x$ contributes only very little to ω_z) develop tongue-like structures (see figure 12 for $t = 10T$), which become more and more elongated as they propagate downstream (compare the first and second structure, figure 12*a*, $t = 10T$). After forming pointed tips, the front (leading) part of the ω_z structures becomes wavy while getting strongly stretched in the downstream direction (figure 12, $t = 10.4T$). The shapes of these structures qualitatively agree with those identified experimentally by Williams *et al.* (1984), who mapped surfaces of constant $\partial u/\partial y$, which supports other findings that the $\partial v/\partial x$ component does not significantly contribute towards ω_z. The shape of the ω_z structures differs from the characteristic Λ-shape that was observed in flow visualization experiments (see Hama & Nutant 1963; Williams *et al.* 1984).

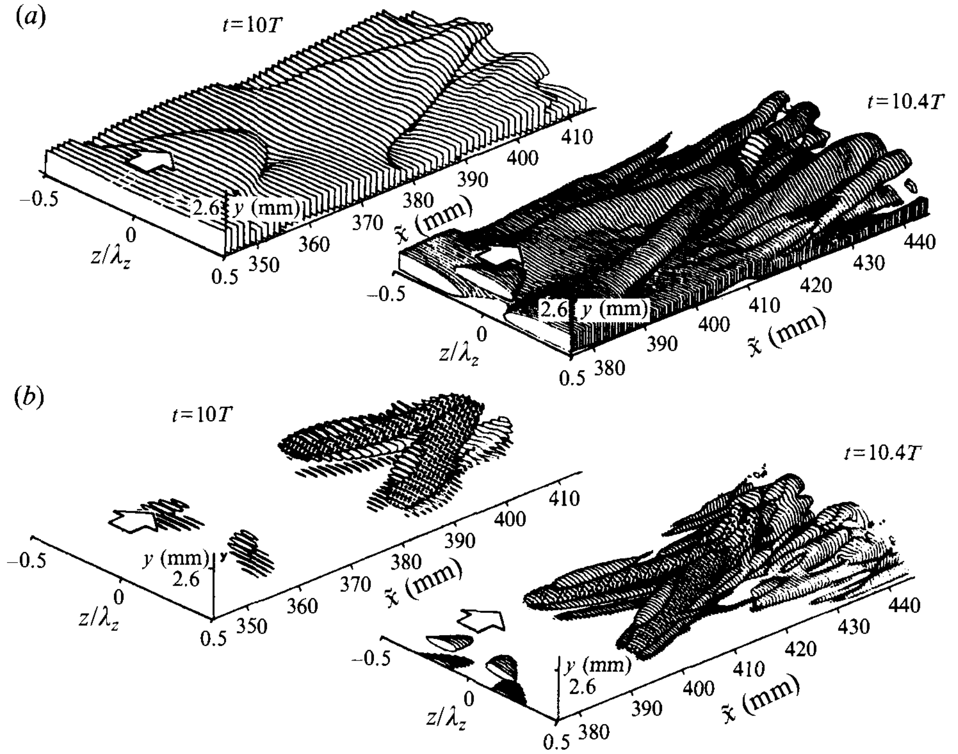

FIGURE 12. Three-dimensional structures identified by surfaces of constant instantaneous ω_z and ω_x for two time instants, $t = 10T$ and $t = 10.4T$: (*a*) $\omega_z = 0.2$; (*b*) $|\omega_x| = 0.05$. The $|\omega_x|$ belonging to a Λ-vortex is marked.

The surfaces of constant $|\omega_x|$ in figure 12, however, identify Λ-shaped structures. These Λ-structures become more and more elongated as they propagate downstream. Later (for $t = 10.4T$), the tip of the Λ-structure lifts up and moves away from the wall while being severely stretched. Of course, the very tip of the vortex cannot be identified by ω_x = constant. This change of position of the Λ-structure relative to the wall can be observed much better in figure 13. Here, contours of constant ω_x are plotted in the (y, z)-plane for several downstream stations. Together with the contours, the projections of the instantaneous velocity vectors onto the (y, z)-plane are also shown for half the cross-section. This instantaneous velocity vector field is shown because in the literature it is often conjectured that the instantaneous velocity field associated with the later three-dimensional transition development could be simply thought of as being induced by the Λ-vortex.

The contours of ω_x = constant in figure 13(*a*) (for $t = 10T$) represent cuts through the second vortex of figure 12(*b*), where the shaded areas mark the Λ-vortex as identified in figure 12(*b*) for $|\omega_x| = 0.05$. Thus, at the first x-station, $\tilde{x} = 388$ mm, we cut through the 'legs' of the vortex; at $\tilde{x} = 399$ mm, we are approximately at the middle of the vortex; at $\tilde{x} = 405$ mm, we are closer to the tip; and, at the last station, $\tilde{x} = 410$ mm, we are practically within or already ahead of the tip since ω_x is very small here. It is very striking how the Λ-vortex, as identified by the contours of the ω_x = constant (shaded) region, changes its shape and orientation from the leg region ($\tilde{x} = 388$ mm) to the tip region. At the leg, the shape is flat with an orientation almost parallel to the wall. Moving towards the tip, the shape changes and becomes oriented

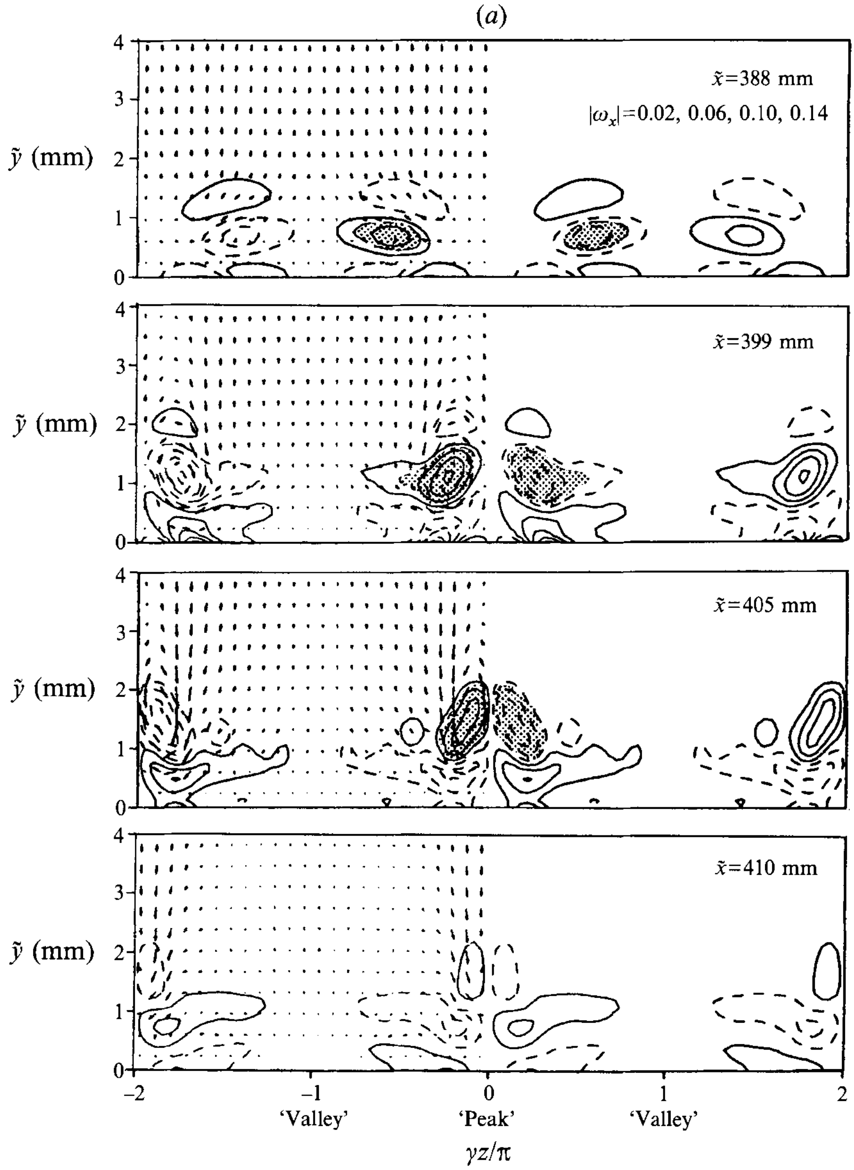

FIGURE 13(a). For caption see facing page.

more and more vertically while moving away from the wall.† In addition to the primary ω_x contours due to the Λ-structure, figure 13(a) also shows contours of secondary vortical structures above and below the primary structures; these structures depict regions of large spanwise shear $\partial w/\partial y$ above and below the primary structures. Based on experimental measurements, Williams *et al.* (1984) suggested that such secondary vortical structures exist, but because of their vicinity to the wall, they were difficult to map out quantitatively. Thus, our simulations clearly support the existence of secondary vortical structures (shear layers) that are directly linked to the primary

† Figure 13, where two periods in the spanwise direction are shown, does not represent the correct aspect ratio of the flow structures. Since the figure covers about 50 mm in the $\tilde{z}$-direction and over 4 mm in the $\tilde{y}$-direction, the $\tilde{y}$-coordinate is stretched by a factor of approximately 4.

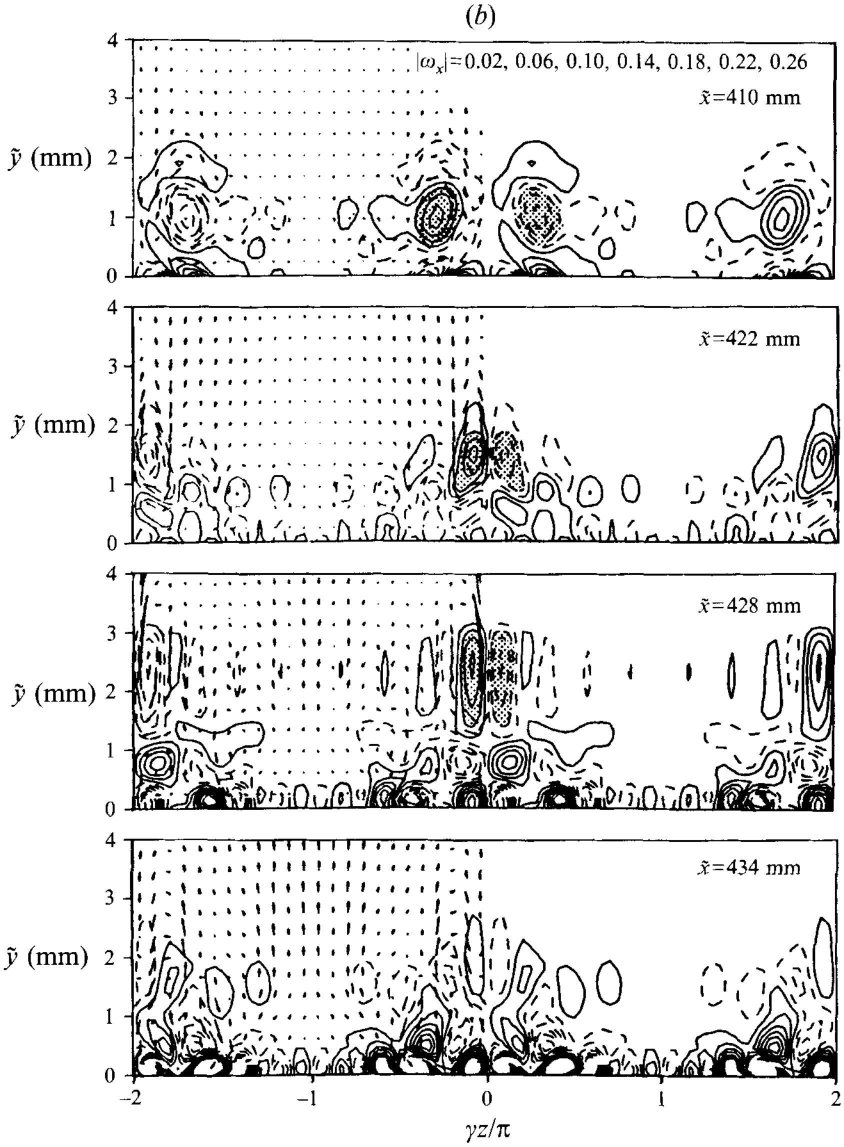

FIGURE 13. Instantaneous velocity field (velocity vectors) and longitudinal vorticity ω_x in planes x = const. for different downstream locations and times: (*a*) 388 mm $\leqslant \tilde{x} \leqslant$ 410 mm, $t = 10T$ (Tollmien–Schlichting period); (*b*) 410 mm $\leqslant \tilde{x} \leqslant$ 434 mm, t = 10.4T. The approximate extent of the Λ-vortex is shaded.

structures. It should be noted that the main contribution to ω_x is from $\partial w/\partial y$ while the $\partial v/\partial z$ contribution is only minor, analogous to the fact that $\partial v/\partial x$ contributes little to ω_z.

Figure 13 shows the effect of insufficient spanwise spectral resolution: grid-scale oscillations with the wavelength of the highest Fourier mode ($k = 8$, i.e. $\lambda_z/8$) at $x = 405$ mm in figure 13(*a*), and throughout figure 13(*b*) (similar plots are available from the (temporal) simulations of Krist & Zang 1987). These oscillations appear to be superimposed on large-amplitude structures which can be thought of being represented by the superposition of spanwise Fourier modes with larger wavelengths.

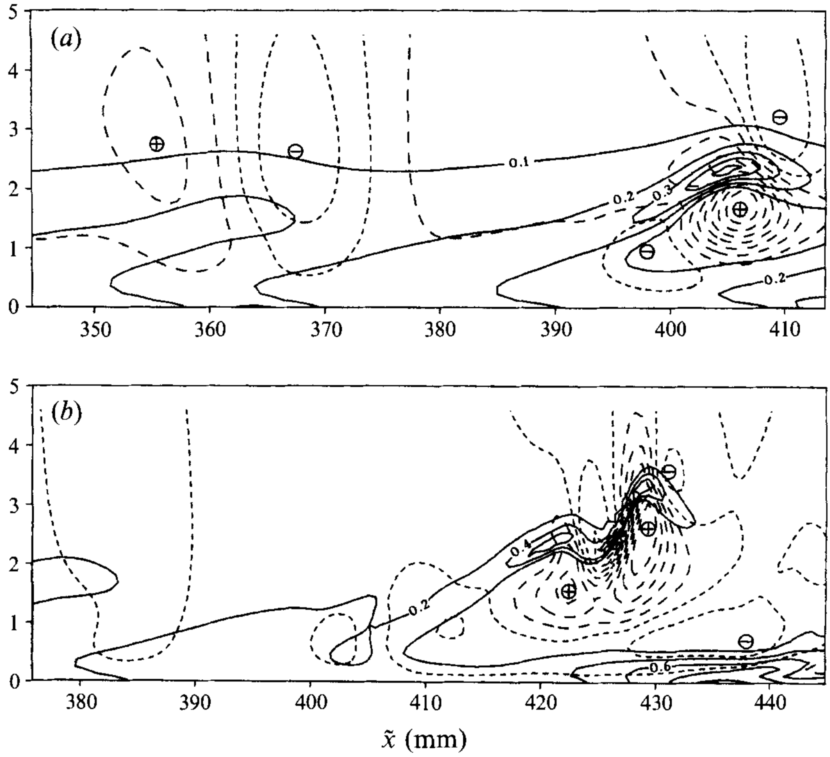

FIGURE 14. Comparison of instantaneous isolines of spanwise ω_z (solid lines) and normal velocity component v (dashed lines) at the peak station ($z = 0$): (*a*) $t = 10T$; (*b*) $t = 10.4T$. Local maxima and minima of v are indicated by ⊕ and ⊖, respectively.

This observation is again consistent with figure 10 where beyond $\tilde{x} = 400$ mm the highest k-modes reached larger amplitudes than the smaller ones without strongly affecting them.

The development of the ω_x contours for the same Λ-structure at a later time than in figure 13(*a*) (and somewhat farther downstream) is demonstrated in figure 13(*b*). Comparison with figure 13(*a*) shows that the structure is considerably more elongated, the cross-sections are farther from the wall, and the orientation in the tip region is considerably more vertical. In addition, the intensities are higher, which can be explained by the stretching in the x-direction. Moreover, in the tip region, secondary vortices and shear layers of high intensity are created below the primary structure and, in particular, right at the wall. The instantaneous velocity vector fields shown together with the ω_x contours in figure 13 do not unequivocally support the notion that the instantaneous velocity field is a consequence of the induction mechanism of the Λ-vortex (because of the discrepancy between velocity vector field and vorticity isolines). This finding is consistent with the fact that secondary vortex structures exist that, of course, will also contribute to the induction mechanism.

On the other hand, we discovered that the behaviour of the high-shear structure in the peak plane appears to be surprisingly consistent with the instantaneous velocity field. For example, in figure 14, the high-shear structure as identified by $\omega_z > 0.4$ in the peak plane is shown together with contours of the instantaneous normal velocity component v. As observed in figure 14(*a*) for $t = 10T$, there is a local maximum of v directly under the forward part of the layer, which would push the structure towards

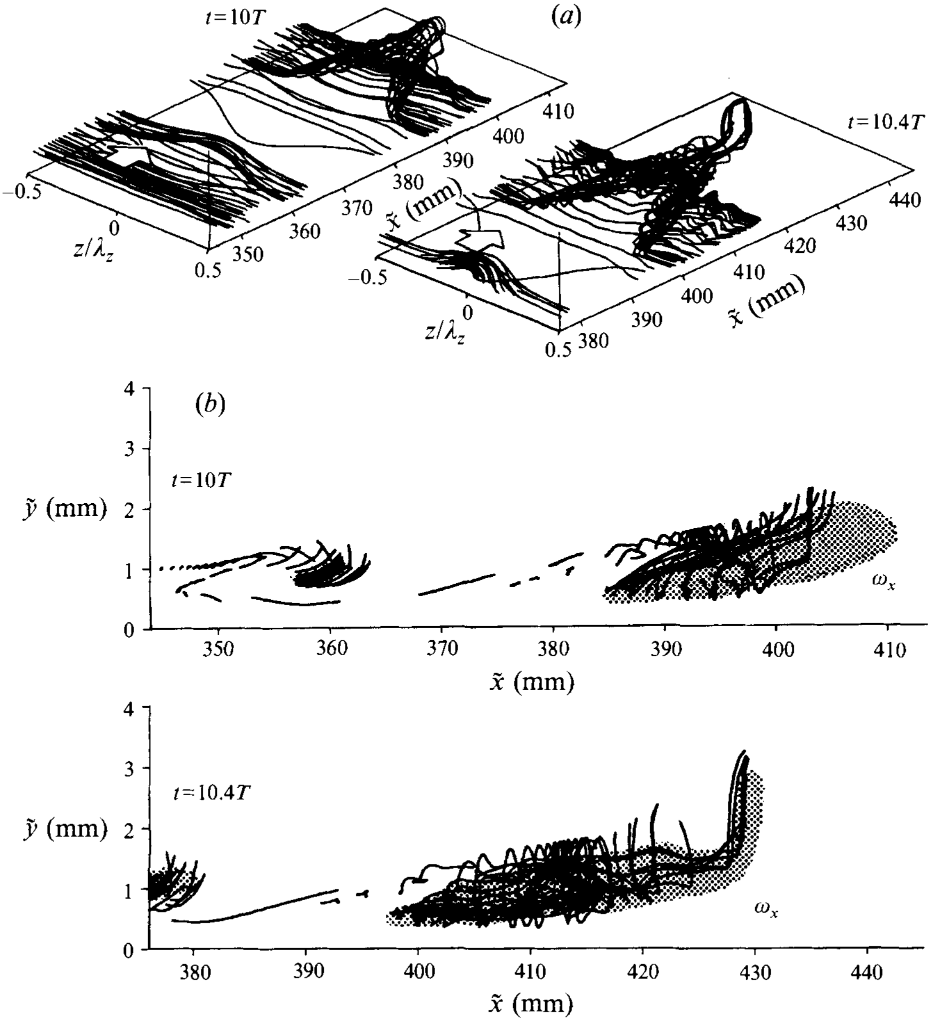

FIGURE 15. Timelines generated by 'marking' wire placed at constant x and y for two time instants, $t = 10T$ and $t = 10.4T$: (*a*) perspective view; (*b*) side view (in the negative z-direction). Shaded area corresponds to the projection of the shaded isosurfaces $|\omega_x| = \text{const.}$ from figure 12(*b*).

the free stream and away from the wall. Above the structure and ahead of the tip, there is a local minimum of v (maximum of negative v-velocity) that tends to push the front of the shear-layer structures towards the wall. Thus the combined action of the v-velocity distribution results in a motion of the structure away from the wall (because the positive maximum below is much stronger than the negative maximum above) and a deformation (bending) of the structure. Even the later development of the shear-layer structure at $t = 10.4T$ in figure 14(*b*) (namely, the complicated change of shape (warping) and the continued uplift) is entirely consistent with the instantaneous v-velocity distribution. Thus, the shear-layer structure in the peak plane is moved and deformed by the instantaneous velocity field like an inertialess entity.

Experimentally, the dominant structures in the transition process are typically identified by flow visualization using hydrogen bubbles or dye. Considering that the interpretation of flow visualization can lead to erroneous results (see, for example, Hama 1962 and Cimbala, Nagib & Roshko 1988), the question arises as to how the structures identified by flow visualization relate to the structures that we have identified from our numerical simulations. To answer this question, we have numerically generated flow visualizations using the data obtained from the simulations. For this, massless marker particles are released in the flow field and their instantaneous position is then determined by the instantaneous velocity field. Figure 15, for example, shows 'timelines' that were generated by releasing particles along a line $x=$ constant and $y=$ constant (particles are released periodically in time), where $\tilde{x}=300$ mm and y corresponds to the location of the critical layer. The timelines at the earlier time instant in figure 15(*a*) for $t=10T$ at first show simply a warping of the Tollmien–Schlichting waves. Farther downstream (the second structure for $t=10T$), the timelines clearly identify a Λ-structure. At the later time (figure 15*a* for $t=10.4T$) and farther downstream, the Λ-structure is strongly elongated in the tip region while the tip (or head) itself is lifting up and, at the same time, forming a hairpin-shaped eddy. These timeline structures closely resemble those observed in experiments using hydrogen bubbles (see, for example, Hama & Nutant 1963; Wortmann 1981; Williams *et al.* 1984).

How do the structures identified by the timelines compare with the Λ-structure identified by surfaces of constant ω_x as in figures 12(*b*) and 13? To answer this question, in figure 15(*b*) the timelines of figure 15(*a*) and the surface of constant ω_x of figure 12(*b*) are superimposed and plotted as a projection on the peak planes. It is obvious that the timelines indeed roughly coincide with the $\omega_x=$ constant structure. (Note that the exact shape and size of the $\omega_x=$ constant structure depends on the chosen constant.) Thus, marker particles get trapped in the Λ-vortex by the action of the ω_x-vorticity.

Another method of identifying the dominant structures in transition experiments is to continuously inject dye at a constant (x,y,z)-location, which thus produces streaklines. What structures are identified by streaklines? Using our numerical data, we produced numerical streaklines by releasing particles at fixed x-, y-, and z-positions and computing their subsequent positions from the instantaneous velocity data. Figure 16 shows the streaklines generated by releasing particles at the spanwise peak station and at three y-locations that were near the critical layer according to linear stability theory. The x-location where the particles were released was at $\tilde{x}=300$ mm. The streaklines are shown together with contours of constant ω_z (the structures of high shear) and the projection of the ω_x-structure ($|\omega_x|=0.05$) onto the peak plane (in order to identify the Λ-vortex structure).

Figure 16 is highly illustrative from several points of view. First, in the early development (the first structure in figure 16*a*), the streaklines (defined by the marker particles) do not correlate with the ω_z contours. However, for the second structure farther downstream, marker particles are entirely concentrated in locations of high ω_z. Even farther downstream, as obvious from figure 16(*b*), for the shear-layer structure at a later time, $t=10.4T$, the particles remain concentrated and trapped in the high-shear layer, even as it undergoes strong deformation and a strong lift-up. Thus, streaklines generated by injecting dye in the peak plane (and near the critical layer) identify the evolution and the later deformation and breakup of the high-shear-layer structure. However, as seen from figure 16, the high-shear-layer structure ($\omega_z=$ constant) and the Λ-vortex (as identified by $\omega_x=$ constant) do not coincide. Rather, the high-shear layer rides on top of the Λ-vortex. This was also suggested by Williams *et al.* (1984) based on their experimental findings. Thus, our simulations support this somewhat surprising finding of the experimental investigation. In addition, our calculations show that the high-shear structure continues to ride on top of the Λ-vortex

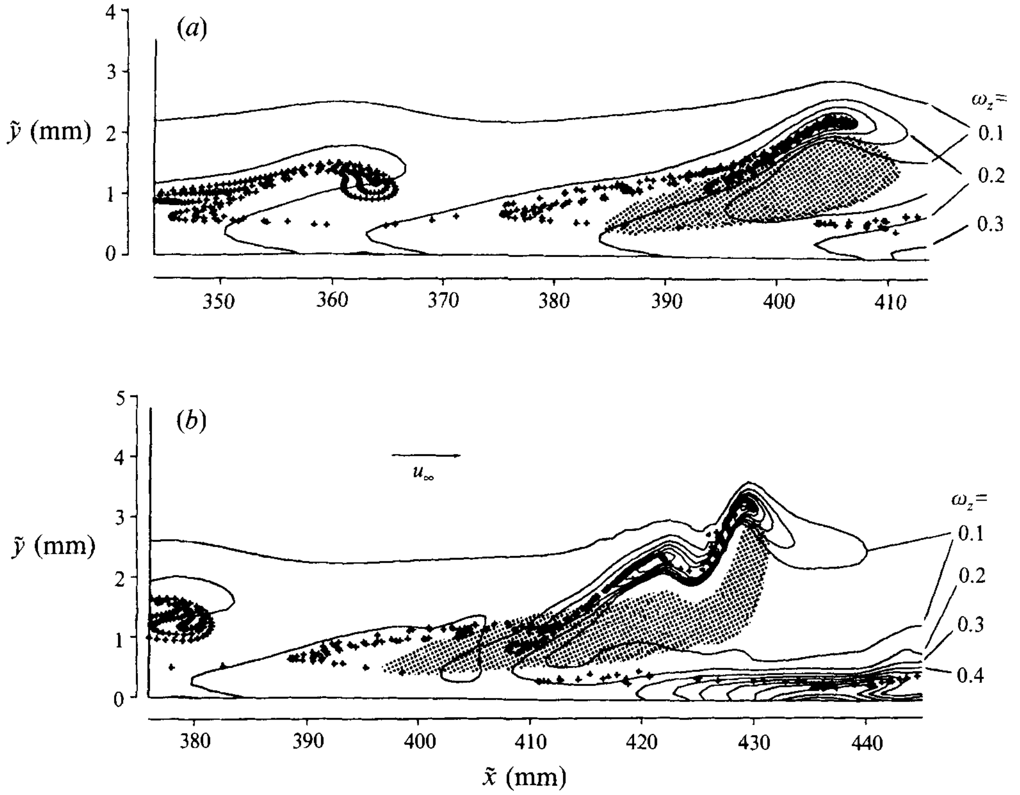

FIGURE 16. Comparison of instantaneous ω_z distribution (isolines) with ω_x concentration (shaded area from figure 12*b*) and marker particles released in the peak plane at $\tilde{x} = 300$ mm (near critical layer): (*a*) $t = 10T$; (*b*) $t = 10.4T$.

even as both structures strongly deform and start to break up in the later three-dimensional development. Therefore, streaklines generated by releasing particles at the peak plane *do not mark* the Λ-vortex, but rather the structures of instantaneous high shear. However, if the marker particles were released off the peak plane, the streakline picture would be different. As seen from figure 15, off-peak particles spiral around the sides of the Λ-vortex and may actually be trapped inside it. Thus, these particles identify the Λ-vortex and not the high-shear layer.

5. Conclusions

A numerical method was developed for solving the complete Navier–Stokes equations that is applicable to direct numerical simulations of laminar–turbulent transition in boundary layers. The method is based on the so-called spatial model, modelling the realistic inflow–outflow geometry as in laboratory experiments. For the numerical method, the Navier–Stokes equations are used in vorticity–velocity formulations, with three vorticity transport equations for the three vorticity components and three Poisson-type equations for the three velocity components. High-order finite differences are employed in the downstream and wall-normal directions, while the spanwise direction is treated pseudospectrally. The method was thoroughly tested by comparison calculations with linear stability theory for both two-dimensional and three-dimensional disturbances and for a subharmonic resonance breakdown. In the present paper, emphasis was placed on simulating the fundamental breakdown in the controlled transition experiments by Kachanov *et al.* (1984, 1985). Toward this end, the parameters in the calculations were selected such that the experimental conditions were closely matched. The results of these simulations agreed remarkably well with measurements up to the second spike station, in spite of relatively coarse resolution in the spanwise direction. In particular, the numerical results confirmed the synchronization of the various wave components within a narrow y-extent that occurs during the spike events. Detailed analysis of the numerical data allowed the identification of the dominant shear layers and vortical structures.

Employing various graphical and flow visualization procedures, the dynamical evolution and breakup of the various structures could be studied in detail. In particular, it was elucidated how different graphical representations and flow visualization techniques (such as streaklines) uncover or obscure certain phenomena and mechanisms. The results of our simulations unequivocally demonstrate that the structures and their dynamical behaviour from the experiments by Kachanov *et al.* (1984, 1985) are similar to those of other controlled fundamental breakdown experiments, such as, for example, those by Klebanoff *et al.* (1962) and Williams *et al.* (1984).

The authors would like to thank the referees for their useful comments and the Deutsche Forschungsgemeinschaft, Bonn-Bad Godesberg for the financial support under contracts Fa 117/2-1, Fa 117/2-2, and Fa 117/2-3. We also gratefully acknowledge the generous support of computer time provided by the University of Stuttgart.

Appendix. Finite-difference approximations

We present here the finite-difference approximations used in our numerical scheme for the discretization of the equations and boundary conditions given in §2. We use the notation $f_{m,n} = F_k(m\Delta y, n\Delta x - x_0, t)$, where F_k stands for the flow variables in Fourier space (after transformation using equation (20)). The indices run from $n = 0$ to N, and from $m = 0$ to M in the x- and y-directions, respectively. For brevity, only those indices that change from grid point to grid point within each equation are written below.

The first derivatives in x (needed for $1 \leqslant m \leqslant M$) are approximated by

$$\left.\frac{\partial f}{\partial x}\right|_{4 \leqslant n \leqslant N-4} = \frac{1}{840\Delta x}(3f_{n-4} - 32f_{n-3} + 168f_{n-2} - 672f_{n-1} + 672f_{n+1} - 168f_{n+2} + 32f_{n+3} - 3f_{n+4}) + O(\Delta x^8),$$

$$\left.\frac{\partial f}{\partial x}\right|_{n=3,\,N-3} = \frac{1}{60\Delta x}(-f_{n-3} + 9f_{n-2} - 45f_{n-1} + 45f_{n+1} - 9f_{n+2} + f_{n+3}) + O(\Delta x^6),$$

$$\left.\frac{\partial f}{\partial x}\right|_{n=2,\,N-2} = \frac{1}{12\Delta x}(f_{n-2} - 8f_{n-1} + 8f_{n+1} - f_{n+2}) + O(\Delta x^4),$$

$$\left.\frac{\partial f}{\partial x}\right|_{n=1} = \frac{1}{2\Delta x}(f_2 - f_0) + O(\Delta x^2),$$

$$\left.\frac{\partial f}{\partial x}\right|_{N-1} = \frac{1}{66\Delta x}(5f_{N-3} - 42f_{N-2} + 3f_{N-1} + (34 + 6\alpha^2\Delta x^2)f_N) + O(\Delta x^4),$$

and

$$\left.\frac{\partial f}{\partial x}\right|_{N} = \frac{1}{66\Delta x}(-4f_{N-3} + 27f_{N-2} - 108f_{N-1} + (85 - 18\alpha^2\Delta x^2)f_N) + O(\Delta x^4).$$

The first derivatives in x at the wall ($m = 0$) are approximated by

$$\left.\frac{\partial \omega_z}{\partial x}\right|_{n=1} = \frac{1}{8\Delta x}\left(-12\omega_{z_0}+12\omega_{z_1}-5\Delta x\left.\frac{\partial \omega_z}{\partial x}\right|_0+\Delta x\left.\frac{\partial \omega_z}{\partial x}\right|_2\right)+O(\Delta x^3),$$

$$\left.\frac{\partial \omega_z}{\partial x}\right|_{2\leqslant n\leqslant N-1} = \frac{1}{14\Delta x}\left(-3\omega_{z_{n-2}}-24\omega_{z_{n-1}}+27\omega_{z_n}-17\Delta x\left.\frac{\partial \omega_z}{\partial x}\right|_{n-1}+\Delta x\left.\frac{\partial \omega_z}{\partial x}\right|_{n+1}\right)$$
$$+O(\Delta x^4),$$

and
$$\left.\frac{\partial \omega_z}{\partial x}\right|_{N} = \frac{1}{\Delta x}\left(-3\omega_{z_{N-2}}+3\omega_{z_N}-\Delta x\left.\frac{\partial \omega_z}{\partial x}\right|_{N-2}-4\Delta x\left.\frac{\partial \omega_z}{\partial x}\right|_{N-1}\right)+O(\Delta x^4),$$

where the $\partial\omega_z/\partial x$-terms on the right-hand sides are known from equation (15).

The second derivatives in x (needed for $1 \leqslant m \leqslant M$) are approximated by

$$\left.\frac{\partial^2 f}{\partial x^2}\right|_{2\leqslant n\leqslant N-2} = \frac{1}{12\Delta x^2}(-f_{n-2}+16f_{n-1}-30f_n+16f_{n+1}-f_{n+2})+O(\Delta x^4),$$

$$\left.\frac{\partial^2 f}{\partial x^2}\right|_{n=1} = \frac{1}{\Delta x^2}(f_0-2f_1+f_2)+O(\Delta x^2),$$

$$\left.\frac{\partial^2 f}{\partial x^2}\right|_{n=N-1} = \frac{1}{11\Delta x^2}(-f_{N-3}+15f_{N-2}-27f_{N-1}+(13+\alpha^2\Delta x^2)f_N)+O(\Delta x^3),$$

and
$$\left.\frac{\partial^2 f}{\partial x^2}\right|_{N} = -(\alpha^2+k^2\gamma^2)f_N \quad \text{(equation (16))}.$$

The first derivatives in y (needed for $1 \leqslant n \leqslant N$) for all flow variables except v at $m = 1$ are approximated by

$$\left.\frac{\partial f}{\partial y}\right|_{2\leqslant m\leqslant M-2} = \frac{1}{12\Delta y}(f_{m-2}-8f_{m-1}+8f_{m+1}-f_{m+2})+O(\Delta y^4),$$

$$\left.\frac{\partial f}{\partial y}\right|_{m=M-1} = \frac{1}{2\Delta y}(f_M-f_{M-2})+O(\Delta y^2),$$

and
$$\left.\frac{\partial f}{\partial y}\right|_{m=1} = \frac{1}{60\Delta y}(-12f_0-65f_1+120f_2-60f_3+20f_4-3f_5)+O(\Delta y^5).$$

For v at $m = 1$, we use the approximation

$$\left.\frac{\partial v}{\partial y}\right|_{m=1} = \frac{1}{48\Delta y}(-37v_0+8v_1+36v_2-8v_3+v_4)+O(\Delta y^5)$$

which takes $\partial v/\partial y\,|_{m=0} = 0$ into account.

The second derivatives in y (needed for $1 \leqslant n \leqslant N$) for all flow variables except v at $m = 1$ are approximated by

$$\left.\frac{\partial^2 f}{\partial y^2}\right|_{2\leqslant m\leqslant M-2} = \frac{1}{12\Delta y^2}(-f_{m-2}+16f_{m-1}-30f_m+16f_{m+1}-f_{m+2})+O(\Delta y^4),$$

$$\left.\frac{\partial^2 f}{\partial y^2}\right|_{m=M-1} = \frac{1}{\Delta y^2}(f_{M-2}-2f_{M-1}+f_M)+O(\Delta y^2),$$

and
$$\left.\frac{\partial^2 f}{\partial y^2}\right|_{m=1} = \frac{1}{12\Delta y^2}(10f_0-15f_1-4f_2+14f_3-6f_4+f_5)+O(\Delta y^4).$$

For v at $m = 1$, we use the approximation

$$\left.\frac{\partial^2 v}{\partial y^2}\right|_{m=1} = \frac{1}{114\Delta y^2}(257v_0 - 480v_1 + 252v_2 - 32v_3 + 3v_4) + O(\Delta y^4).$$

Directly at the wall, we need the approximations

$$\left.\frac{\partial w}{\partial y}\right|_{m=0} = \frac{1}{60\Delta y}(-137w_0 + 300w_1 - 300w_2 + 200w_3 - 75w_4 + 12w_5) + O(\Delta y^5),$$

and $$\left.\frac{\partial^2 v}{\partial y^2}\right|_{m=0} = \frac{1}{72\Delta y^2}(-415v_0 + 576v_1 - 216v_2 + 64v_3 - 9v_4) + O(\Delta y^4).$$

REFERENCES

Bertolotti, F. P. 1991 Linear and nonlinear stability of boundary layers with streamwise varying properties. Dissertation, Ohio State University.

Bertolotti, F. P., Herbert, Th. & Spalart, P. R. 1992 Linear and nonlinear stability of the Blasius boundary layer. *J. Fluid Mech.* **242**, 441–474.

Biringen, S. 1987 Three-dimensional vortical structures of transition in plane channel flows. *Phys. Fluids* **30**, 3359–3368.

Cimbala, F. M., Nagib, H. M. & Roshko, A. 1988 Large structures in the far wakes of two-dimensional bluff bodies. *J. Fluid Mech.* **190**, 265–298.

Fasel, H. F. 1976 Investigation of the stability of boundary layers by a finite-difference model of the Navier–Stokes equations. *J. Fluid Mech.* **18**, 355–383.

Fasel, H. F. & Konzelmann, U. 1990 Non-parallel stability of a flat plate boundary layer using the complete Navier–Stokes equations. *J. Fluid Mech.* **221**, 311–347.

Fasel, H. F., Rist, U. & Konzelmann, U. 1990 Numerical investigation of the three-dimensional development in boundary-layer transition. *AIAA J.* **28**, 29–37.

Gaster, M. 1962 A note on the relation between temporally-increasing and spatially-increasing disturbances in hydrodynamic stability. *J. Fluid Mech.* **14**, 222–224.

Gaster, M. 1965*a* On the generation of spatially growing waves in a boundary layer. *J. Fluid Mech.* **22**, 433–441.

Gaster, M. 1965*b* The role of spatially growing waves in the theory of hydrodynamic stability. *Prog. Aerospace Sci.* **6**, 251–270.

Gaster, M. 1968 Growth of disturbances in both space and time. *Phys. Fluids* 11, 723–727.

Gaster, M. 1974 Nonparallel effects on boundary layer stability. *J. Fluid Mech.* **66**, 465–480.

Gaster, M. & Grant, I. 1975 An experimental investigation of the formation and development of a wave packet in a laminar boundary layer. *Proc. R. Soc. Lond.* A **341**, 253–269.

Hama, F. R. 1962 Streaklines in a perturbed shear flow. *Phys. Fluids* **5**, 644–650.

Hama, F. R. & Nutant, J. 1963 Detailed flow-field observations in the transition process in a thick boundary layer. In *Proc. 1963 Heat Transfer and Fluid Mech. Inst.*, pp. 77–93. Stanford University Press.

Heisenberg, W. 1924 Über Stabilität und Turbulenz von Flüssigkeitsströmen. *Ann. Phys.* **74**, 577–627.

Herbert, T. 1988 Secondary instability of boundary layers. *Ann. Rev. Fluid Mech.* **20**, 487–526.

Huerre, P. & Monkewitz, P. A. 1990 Local and global instabilities in spatially developing flows. *Ann. Rev. Fluid Mech.* **22**, 473–537.

Jordinson, R. 1970 The flat plate boundary layer. Part 1. Numerical integration of the Orr–Sommerfeld equation. *J. Fluid Mech.* **43**, 801.

KACHANOV, Y. S. 1987 On the resonant nature of the breakdown of a laminar boundary layer. *J. Fluid Mech.* **184**, 43–74.

KACHANOV, Y. S., KOZLOV, V. V. & LEVCHENKO, V. Y. 1977 Nonlinear development of a wave in a boundary layer. *Izv. Akad. Nauk, SSSR Mech. Zhid Gaza* 3, 49–53 (in Russian); (transl. *Fluid Dyn.* **12**, 1987, 383–390).

KACHANOV, Y. S., KOZLOV, V. V., LEVCHENKO, V. Y. & RAMAZANOV, M. P. 1984 Experimental study of K-regime of breakdown of laminar boundary layer. *Preprint* 9-84. Novosibirsk, ITPM SO AN SSSR (in Russian).

KACHANOV, Y. S., KOZLOV, V. V., LEVCHENKO, V. Y. & RAMAZANOV, M. P. 1985 On the nature of K-breakdown of a laminar boundary-layer; new experimental data. In *Laminar–Turbulent Transition* (ed. V. V. Kozlov), pp. 61–73. Springer.

KACHANOV, Y. S. & LEVCHENKO, V. Y. 1984 The resonant interaction of disturbances at laminar–turbulent transition in a boundary layer. *J. Fluid Mech.* **138**, 209–247.

KLEBANOFF, P. S., TIDSTROM, K. D. & SARGENT, L. M. 1962 The three-dimensional nature of boundary-layer instability. *J. Fluid Mech.* **12**, 1–34.

KLEISER, L. 1982 Numerische Simulation zum laminar-turbulenten Umschlagsprozeß der ebenen Poiseuille-Strömung. Dissertation, University of Karlsruhe.

KLEISER, L. & ZANG, T. A. 1991 Numerical simulation of transition in wall-bounded shear flows. *Ann. Rev. Fluid Mech.* **23**, 495–537.

KLOKER, M., KONZELMANN, U. & FASEL, H. 1993 Outflow boundary conditions for spatial Navier–Stokes simulations of transitional boundary layers. *AIAA J.* **31**, 620–628.

KONZELMANN, U., RIST, R. & FASEL, H. 1987 Erzeugung dreidimensionaler, räumlich angefachter Störwellen durch periodisches Ausblasen und Absaugen in einer Plattengrenzschichtströmung. *Z. Angew. Math. Mech.* **67**, T298–T300.

KOVASZNAY, L. S. G., KOMODA, H. & VASUDEVA, B. R. 1962 Detailed flow field in transition. In *Proc. 1962 Heat Transfer and Fluid Mech. Inst.*, pp. 1–26, Stanford University Press.

KOZLOV, V. V. & LEVCHENKO, V. Y. 1987 Laminar-turbulent transition controlled by localized disturbances. In *Turbulence Management and Relaminarization* (ed. H. W. Liepmann & R. Narasimha), pp. 249–269. Springer.

KRIST, S. E. & ZANG, T. A. 1987 Numerical simulation of channel flow transition. Resolution requirements and structure of the hairpin vortex. *NASA TP* 2667.

LAURIEN, E. & KLEISER, L. 1989 Numerical simulation of boundary-layer transition and transition control. *J. Fluid Mech.* **199**, 403–440.

RAI, M. M. & MOIN, P. 1991 Direct simulations of turbulent flow using finite-difference schemes. *J. Comput. Phys.* **96**, 15–53.

RAI, M. M. & MOIN, P. 1993 Direct simulations of transition and turbulence in a spatially evolving boundary layer. *J. Comput. Phys.* **109**, 169–192.

RIST, U. 1990 Numerische Untersuchung der räumlichen, dreidimensionalen Störungsentwicklung beim Grenzschichtumschlag. Dissertation, University of Stuttgart.

ROACHE, P. J. 1976 *Computational Fluid Dynamics.* Hermosa, Albuquerque.

SCHLICHTING, H. 1933 Zur Entstehung der Turbulenz bei der Plattenströmung. *Z. Angew. Math. Mech.* **13**, 171–174.

SCHMIDT, P. J. & HENNINGSON, D. S. 1992 A new mechanism for rapid transition involving a pair of oblique waves. *Phys. Fluids* A **4**, 1986–1989.

SCHUBAUER, G. B. & SKRAMSTAD, H. K. 1947 Laminar boundary layer oscillations and stability of laminar flow. *J. Aeronaut. Sci.* **14**, 69–78.

SPALART, P. R. & YANG, K. S. 1987 Numerical study of ribbon-induced transition in Blasius flow. *J. Fluid Mech.* **118**, 345–365.

TOLLMIEN, W. 1929 Über die Entstehung der Turbulenz; 1. Mitteilung. *Nachr. Ges. Wiss. Göttingen, Math. Phys. Klasse*, pp. 21–44.

WILLIAMS, D. R., FASEL, H. F. & HAMA, F. R. 1984 Experimental determination of the three-dimensional vorticity field in the boundary-layer transition process. *J. Fluid Mech.* **149**, 179–203.

WORTMANN, F. X. 1981 Boundary-layer waves and transition. In *Advances in Fluid Mechanics* (ed. E. Krause). Lecture Notes in Physics, vol. 148, pp. 268–279. Springer.

WRAY, A. & HUSSAINI, M. Y. 1984 Numerical experiments in boundary-layer stability. *Proc. R. Soc. Lond.* A **392**, 373–389.

ZANG, T. A. & HUSSAINI, M. Y. 1987 Numerical simulation of nonlinear interactions in channel and boundary-layer transition. In *Nonlinear Wave Interactions in Fluids* (ed. R. W. Miksad, T. R. Akylas & T. Herbert), pp. 131–145. AMD-87, ASME.